

# Isotropy and Gaussianity of the CMB

Enrique Martínez-González

Instituto de Física de Cantabria, Santander (Spain)  
On behalf of the Planck collaboration

# Outline

- Standard cosmological model
- Beyond the standard model
  - Non-standard inflationary models
  - Topological defects
  - Geometry and topology
  - Primordial magnetic fields
- Planck data and simulations
- Contaminants and Secondary anisotropies:
  - Galactic foregrounds
  - Extragalactic sources
  - Combined ISW-lensing effect
- Tests of Gaussianity
- WMAP anomalies revisited
- Next steps: polarization
- Summary

# Standard Cosmological Model

- FLRW solution of the Einstein field equations:
  - Homogeneous and isotropic metric with an expanding scale factor of the universe. Four periods of evolutions:
    - Accelerated expansion: Inflation
    - Radiation dominated
    - Matter dominated: dark matter + baryons
    - Accelerated expansion: dark energy
  - Cosmological inflation: accelerated expansion at very early times driven by the inflaton. Properties:
    - Present density inhomogeneities originate from quantum fluctuations of the inflaton.
    - Inflaton fluctuations are Gaussian
    - Temperature fluctuations are related to the inflaton fluctuations by linear theory and then preserves their Gaussian character.

# Temperature anisotropies

- The CMB temperature anisotropies can be decomposed in terms of the spherical harmonic coefficients:

$$\frac{\Delta T}{T} \left( \vec{n} \right) = \sum_{\ell,m} a_{\ell m}^T Y_{\ell m} \left( \vec{n} \right)$$

- An important statistical quantity is the CMB (rotationally invariant) power spectrum which is defined as:

$$C_\ell = \left\langle \left| a_{\ell m}^T \right|^2 \right\rangle \text{ and it is estimated from a map as } C_\ell = \frac{1}{2\ell+1} \sum_m \left| a_{\ell m}^T \right|^2$$

- For polarization the Q,U Stokes parameters are usually transformed in the scalar quantities E,B modes as follows:

$$(Q + iU) \left( \vec{n} \right) = \sum_{\ell,m} a_{\ell m}^{(\pm 2)} {}_{\pm 2} Y_{\ell m} \left( \vec{n} \right)$$

$$a_{\ell m}^E \equiv -\frac{1}{2} \left( a_{\ell m}^{(2)} + a_{\ell m}^{(-2)} \right), a_{\ell m}^B \equiv -\frac{1}{2i} \left( a_{\ell m}^{(2)} - a_{\ell m}^{(-2)} \right)$$

$$E \left( \vec{n} \right) = \sum_{\ell m} a_{\ell m}^E Y_{\ell m} \left( \vec{n} \right), B \left( \vec{n} \right) = \sum_{\ell m} a_{\ell m}^B Y_{\ell m} \left( \vec{n} \right)$$

# Isotropic Gaussian Random Field

- Definition of a Gaussian Random Field  $y(\vec{r})$ :
  - For any set of n points  $\vec{r}_1, \vec{r}_2, \dots, \vec{r}_n$  the n-point  $y_1, y_2, \dots, y_n$  probability density function of the random field on those points is an n-point multinomial distribution:
$$f(y_1, y_2, \dots, y_n) = \frac{1}{(2\pi)^{n/2} |M|^{1/2}} \exp \sum_{ij} (y_i - \bar{y}_i) M_{ij}^{-1} (y_j - \bar{y}_j)$$
where  $M_{ij} = \langle (y_i - \bar{y}_i)(y_j - \bar{y}_j) \rangle$ . In the case of the CMB anisotropies, the support is the sphere and the points are directions on the sky.
- Statistical isotropy:
  - The CMB anisotropies are said to be statistically isotropic if for any pair of points:
$$\langle y(\vec{r}_1) y(\vec{r}_2) \rangle = C(|\vec{r}_1 - \vec{r}_2|) \quad \langle a_{\ell m} a_{\ell' m'}^* \rangle = \delta_{\ell'}^{\ell} \delta_{m'}^m C_{\ell}$$

# Cosmic Variance

The power spectrum  $C_l$  and the correlation function  $C(\theta)$  are related by the Legendre transformation:

$$C(\theta) \equiv \left\langle \frac{\Delta T}{T}(\vec{n}_1) \frac{\Delta T}{T}(\vec{n}_2) \right\rangle = \sum_l \frac{2l+1}{4\pi} C_l P_l(\cos \theta)$$

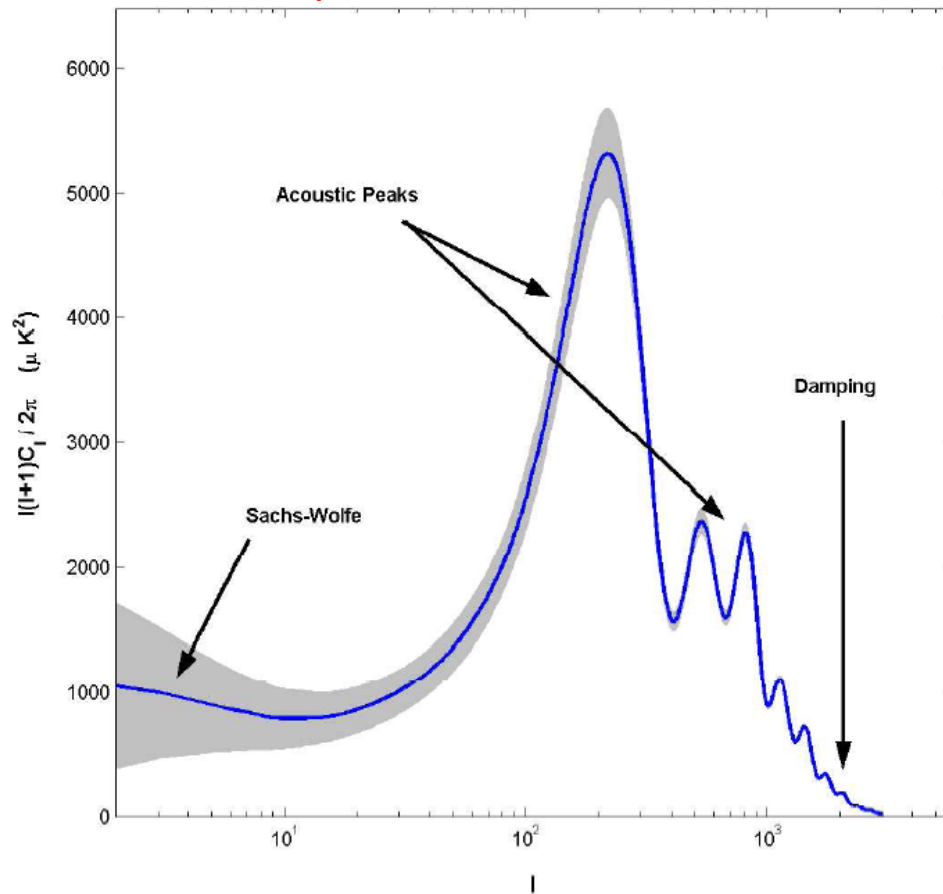
where  $C_l \equiv \frac{1}{2l+1} \sum_{m=-l}^l |a_{lm}|^2$

For an IGRF it is possible to get the variance of the power spectrum  $C_l$  in an analytical form:

$$\Delta C_l = \frac{1}{\sqrt{l+0.5}} C_l$$

This is the dispersion of a  $\chi^2$  distribution with  $2l+1$  dof.

# CMB science: $C_l$ information



Planck has provided a nearly cosmic-variance-limited  $C_l$  in the multipole range  $2 < l < 2000$  where primary anisotropies dominate.

# Probing isotropy and Gaussianity

- Planck and the next generation of CMB polarization missions (e.g. PRISM) will probe two important features of the current cosmological paradigm: the isotropy of the universe and the isotropy and Gaussianity of the primordial perturbations.
- There are two main approaches for testing the Isotropy and Gaussianity of the CMB:
  - Performing non-directional tests of the null hypothesis
  - Performing tests of alternative hypotheses
- There are many physical effects that might give rise to different deviations from isotropy and/or Gaussianity. The deviations might be classified according to their physical nature and origin as follows:
  - Primordial Non-Gaussianity (see Bartjan Van Tent's talk)
  - Topological defects: cosmic strings, textures, ...
  - Geometry and topology: Bianchi models, non-trivial topologies
  - Primordial magnetic fields (see Daniela Paoletti's talk)

# Tests of the null hypothesis

- Before Planck there have been many tests of the null hypothesis (isotropy and Gaussianity) mainly based on the WMAP data. Although the two properties are very much tighten together, some tests try to focus on one property more than the other.
- Several analyses of the WMAP data using different statistical quantities have found deviations from the null hypothesis, what are generally known as WMAP anomalies. Some of the best studied ones are:
  - Low multipole alignment
  - Hemispherical asymmetry
  - The cold spot
  - Low variance
- Planck has represented a unique opportunity to confirm or reject those anomalies
- Results based on the temperature data of the nominal mission have been made public in the March 2013 release.
- Next results based in the temperature and polarization of the whole mission expected for mid-2014 .

# Validate the Gaussianity assumption for the power spectrum and parameters estimation

- The confirmation of the isotropic and Gaussian nature of the CMB is essential to justify the corresponding assumptions usually made in the estimation of the power spectra and cosmological parameters.
- The detection of significant deviations from those assumptions, no compatible with known systematics or foreground residuals, would require major revision of current methodological approaches for the derivation of the mission's main science results.

# Gaussianity and Isotropy Planck Papers

Planck 2013 results  
XXIV

Constraints on primordial  
non-Gaussianity

Planck 2013 results  
XXV

Searches for cosmic  
strings and other  
topological defects

Planck 2013 results  
XXIII

Isotropy and statistics  
of the CMB

Planck 2013 results  
XIX

The integrated Sachs-  
Wolfe effect

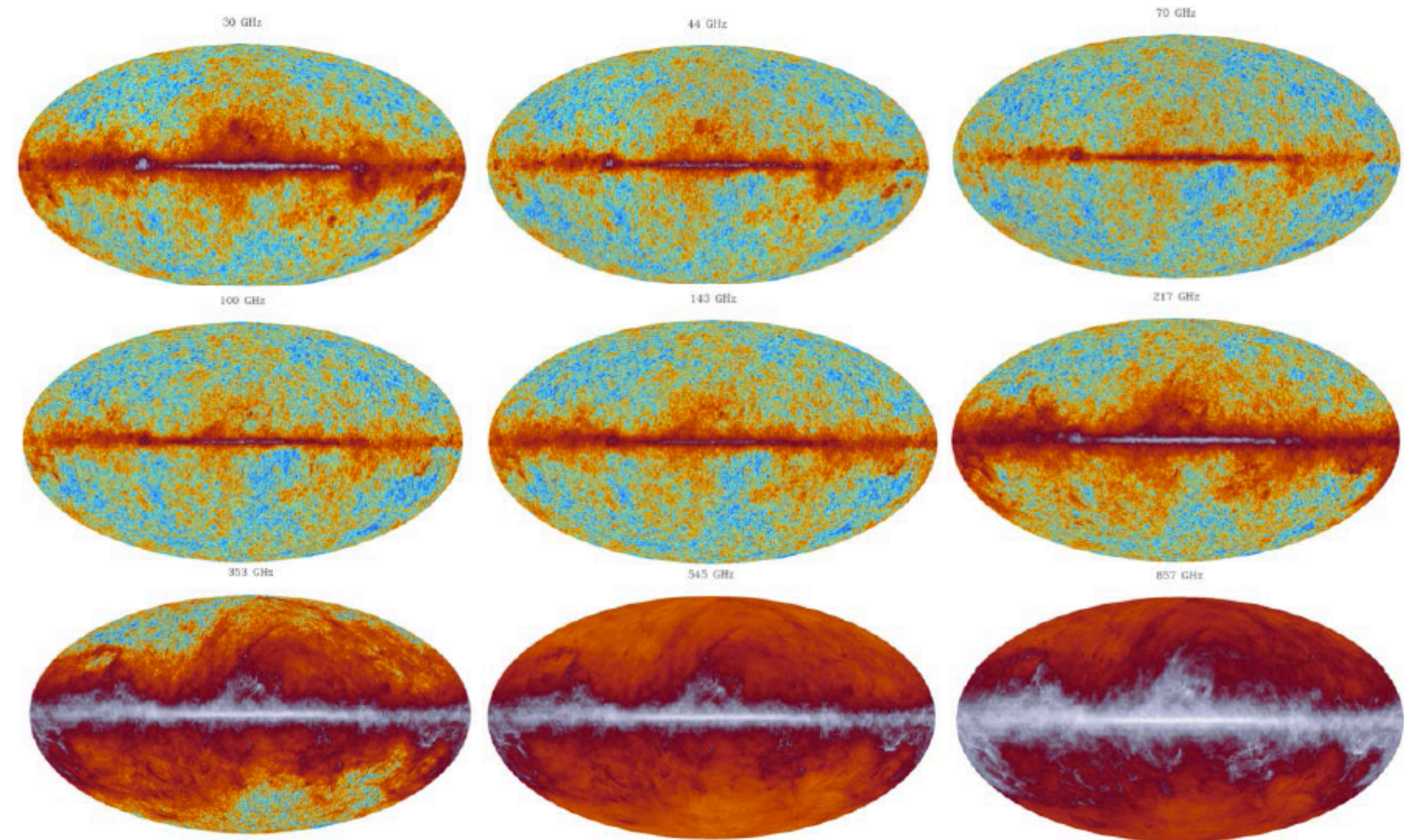
Planck 2013 results  
XXVI

Background geometry  
and topology of the  
Universe

# Planck data

- Nominal mission
- Frequency maps
- Four different clean CMB maps
- Different masks
- Control of foreground residuals
- Control of systematics
- Secondary anisotropies

# PLANCK FREQUENCY MAPS

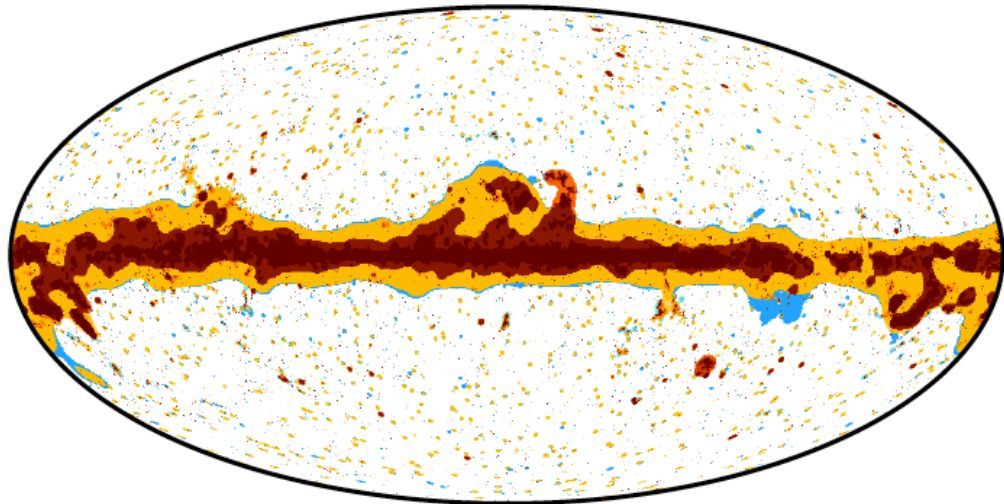


# Main sources of contamination

- **Galactic emissions:**

- Diffuse anisotropic emissions from synchrotron, free-free, thermal dust, spinning dust.
- Component separation methods make use of the Planck frequency coverage to reduce them.
- The intense Galactic plane is masked.

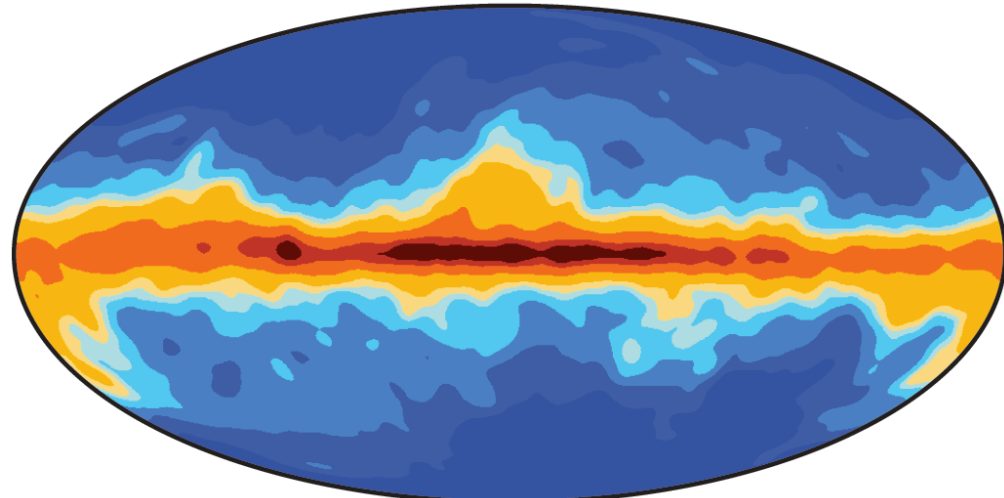
Common mask (U73)



- **Extragalactic sources:**

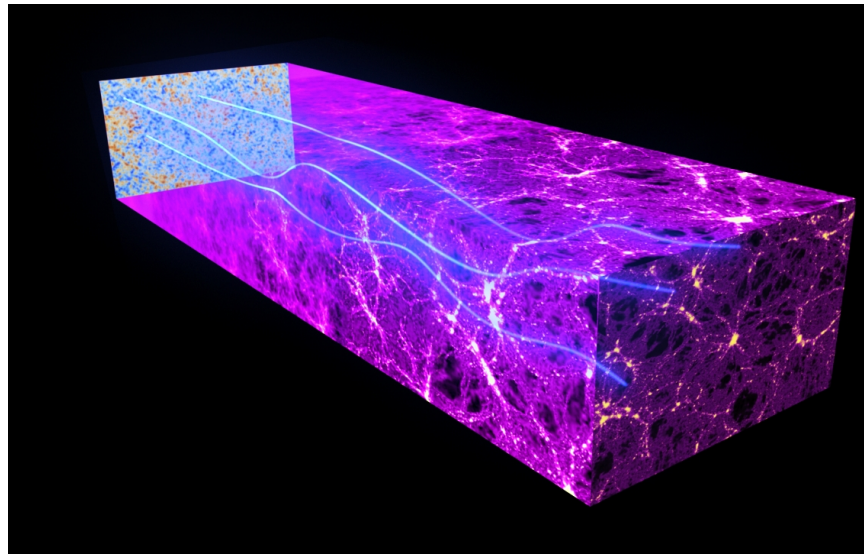
- Point-like emissions from radio and IR sources with an isotropic distribution
- The brightest sources are detected and masked.
- Their effect is clearly seen in the Planck spectrum and bispectrum.

Galactic masks (30+353 GHZ combination)

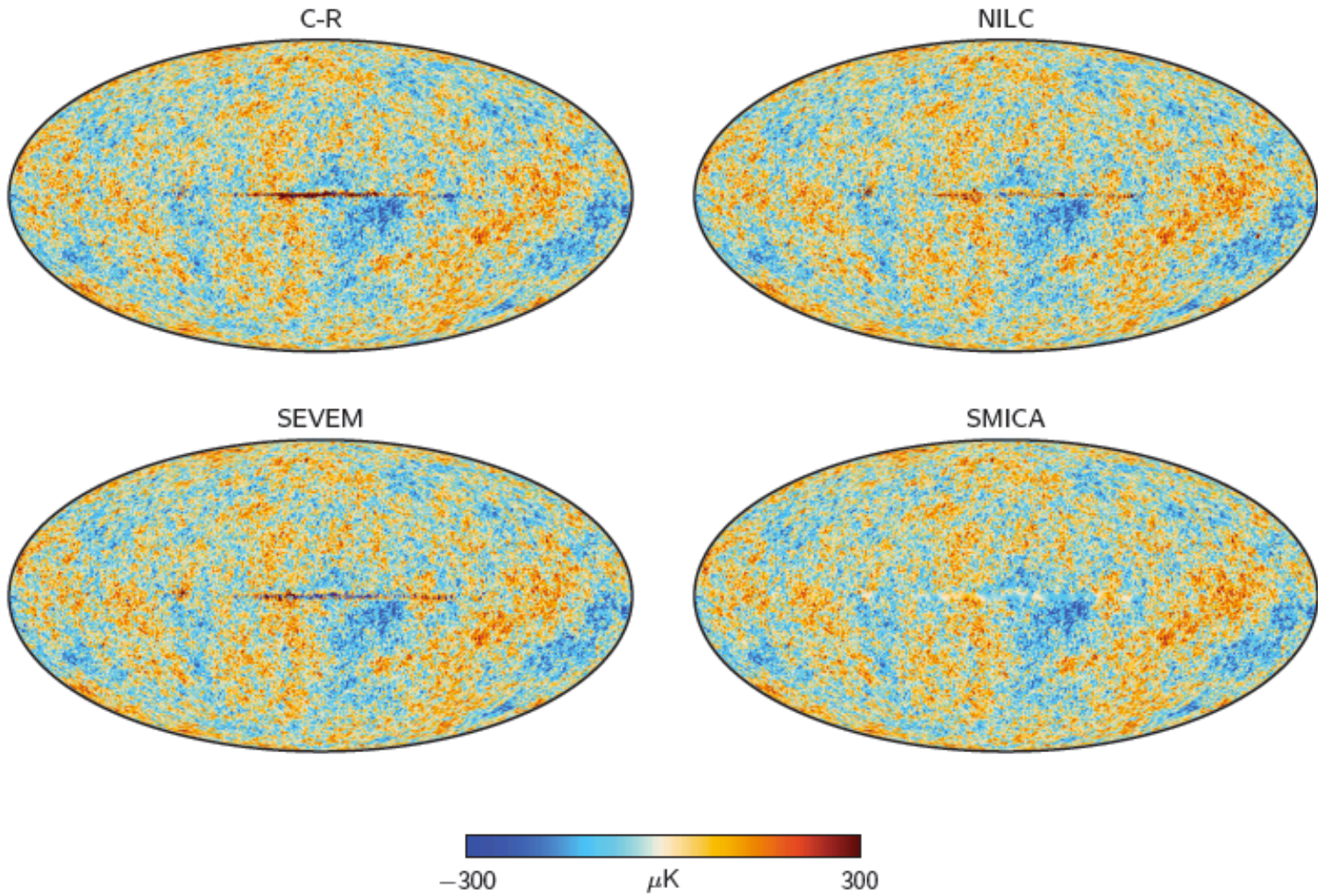


# Secondary anisotropies

- Combined ISW-lensing effect:
  - The same potentials that produce the ISW effect (redshift) also bend the photons (lensing).
  - The signal is detected in the Planck bispectrum at  $\approx 2.5\sigma$  (see Patricio Vielva's talk)
- SZ effect:
  - Inverse Compton scattering off the CMB photons clearly seen towards galaxy clusters.
  - It can be separated from the CMB via its genuine frequency dependence.



# Foreground-cleaned CMB maps



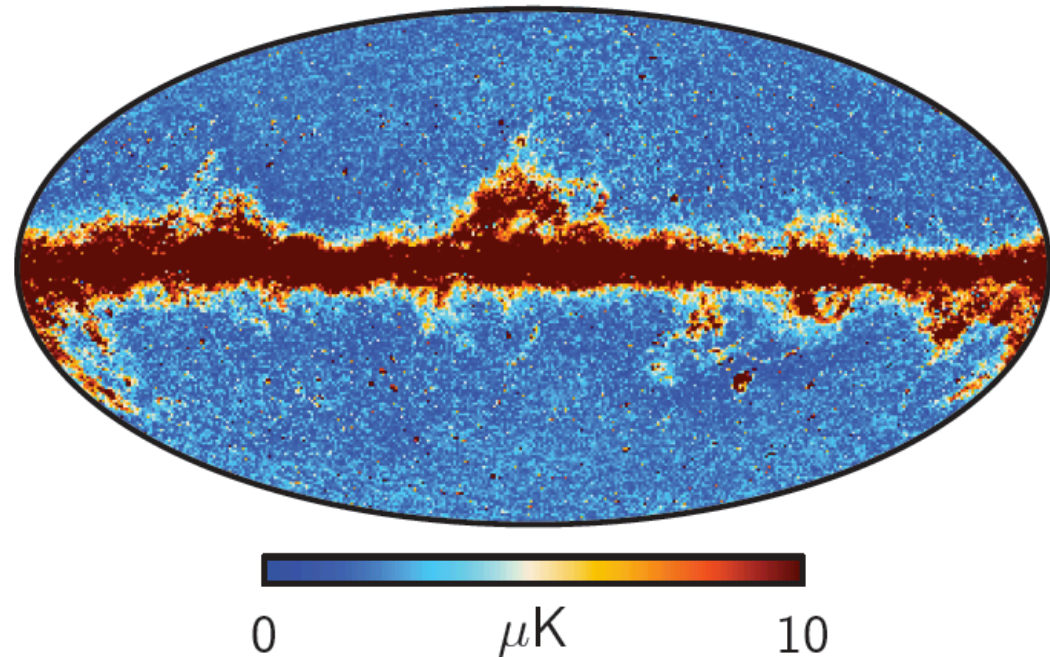
SMICA works in harmonic space; it uses a 3% processing mask to prevent foreground leakage from low to high Galactic latitudes, hence the smooth appearance in the Galactic plane

# Simulations

- Realistic Planck simulations (FFP6):

- Instrumental level:
    - Scanning strategy
    - Telescope
    - Detector responses
    - Data reduction pipeline
  - Microwave sky model (PSM):
    - Galactic emissions
    - Extragalactic emissions

1- $\sigma$  deviation of the four foreground-cleaned CMB maps



- Monte Carlo simulations:

- Best-fit Planck CMB power spectrum used
  - Four sets of maps mimicking the four component separation pipelines.

# Further checks on systematics

Most of the analyses have been thoroughly tested against systematics introduced by foreground residuals:

- The raw maps at 70GHz, 100GHz, 143GHz and 217GHz
- The clean maps at 70GHz, 100GHz, 143GHz and 217GHz produced by SEVEM
- Corresponding CMB and noise simulations (FFP6):
  - including lensing
  - instrumental error propagated from the frequency channels
  - beam propagated from in flight main beams measurements
- A suite of galactic masks, including those used for the Planck likelihood

# Are the primordial fluctuations Gaussian and isotropic?

- Previous attempts based mainly on WMAP
- Planck represents a unique opportunity with cosmic variance sensitivity up to and minimum foreground contamination
- No unique signature of non-Gaussianity
- Broad range of statistical tools with complementary statistical properties of the null hypothesis in real, harmonic and wavelet spaces:
  - One dimensional moments
  - N-pdf
  - N-point correlation functions
  - Minkowski functionals
  - Wavelet statistics
  - Bispectrum

# One dimensional moments

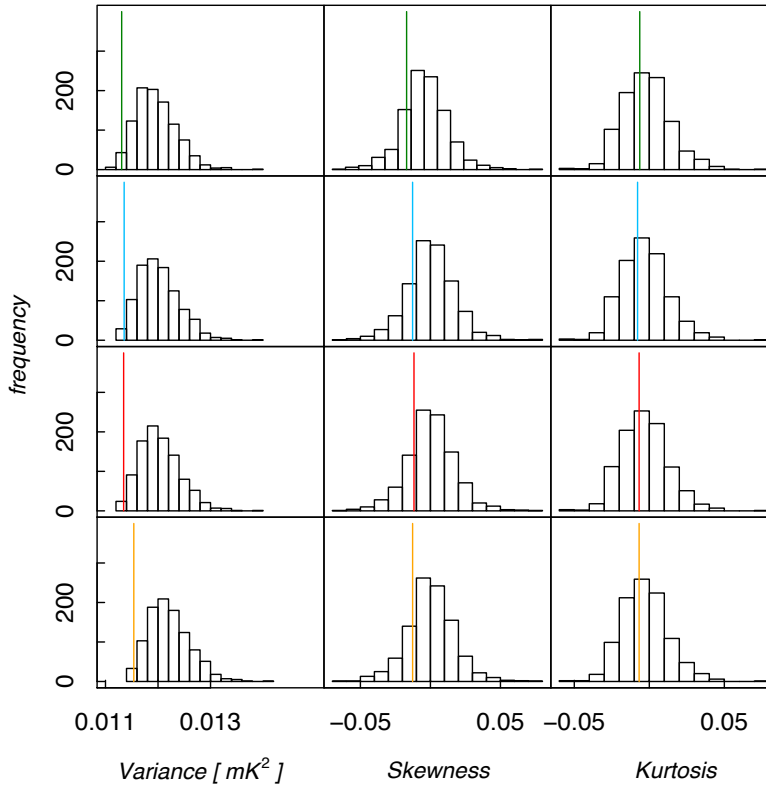


**Fig. 1.** Variance, skewness and kurtosis for the combined map of the four different component separation methods. From top row to bottom row C-R, NILC, SEVEM, SMICA.

**Table 2.** Lower tail probability for the variance, skewness and kurtosis estimators at  $N_{\text{side}} = 2048$ , using the U73 mask and four different component separation methods.

Method	Variance	Skewness	Kurtosis
C-R . . . . .	0.021	0.189	0.416
NILC . . . . .	0.020	0.191	0.392
SEVEM . . . . .	0.014	0.206	0.419
SMICA . . . . .	0.017	0.189	0.419

**Table 3.** Lower tail probability for the variance, skewness and kurtosis estimators at  $N_{\text{side}} = 2048$ , for the SMICA method, using different masks.

Mask	Variance	Skewness	Kurtosis
U73, $f_{\text{sky}} = 73\% \dots \dots \dots$	0.017	0.189	0.419
CL58, $f_{\text{sky}} = 58\% \dots \dots \dots$	0.003	0.170	0.363
CL37, $f_{\text{sky}} = 37\% \dots \dots \dots$	0.030	0.314	0.266
Ecliptic North, $f_{\text{sky}} = 36\% \dots \dots$	0.001	0.553	0.413
Ecliptic South, $f_{\text{sky}} = 37\% \dots \dots$	0.483	0.077	0.556



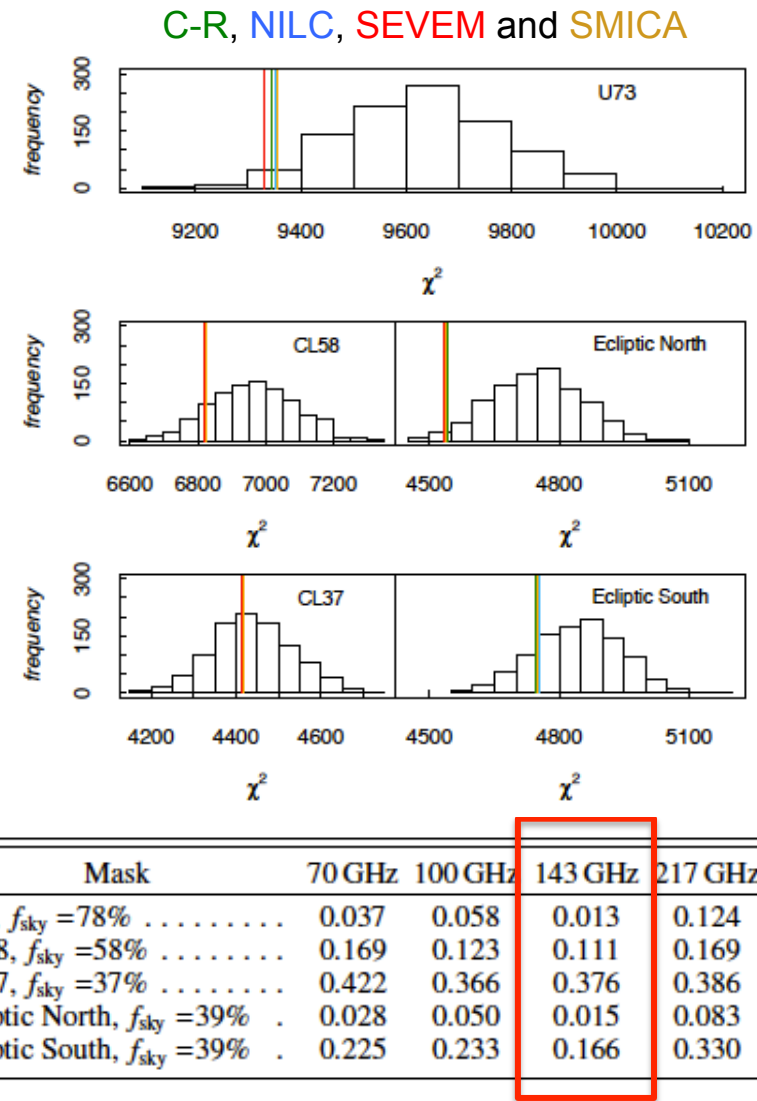
Relation with the low variance (e.g., Cruz et al. 2011) and hemispherical asymmetry (e.g., Hansen 2004) anomalies

# N-pdf

$$f(\mathbf{T}) = \frac{1}{(2\pi)^{N_{pix}/2} \det \mathbf{C}^{1/2}} \exp -\frac{1}{2} (\mathbf{T} \mathbf{C}^{-1} \mathbf{T}^T),$$

$$C_{ij} = \sum_{\ell=0}^{\ell_{\max}} \frac{2\ell+1}{4\pi} C_\ell b_\ell^2 P_\ell(\cos \theta_{ij})$$

Unfeasible at  $N_{\text{side}} = 2048 \rightarrow$  Analysis done at  $N_{\text{side}} = 32$

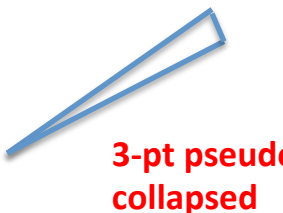


Connection with the hemispherical asymmetry anomaly

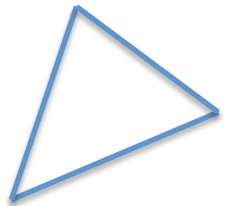
# N-point correlation function

For an isotropic field, the N-point correlation function computed as averages over pixels forming a given polynomial shape, do not depend neither of the position of the shape nor on its orientation.

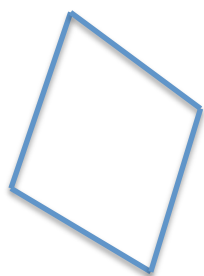
$$C_N(\theta_1, \dots, \theta_{2N-3}) = \frac{\sum_i (w_1^i \cdots w_N^i) (\Delta T_1^i \cdots \Delta T_N^i)}{\sum_i w_1^i \cdots w_N^i}$$



3-pt pseudo-collapsed



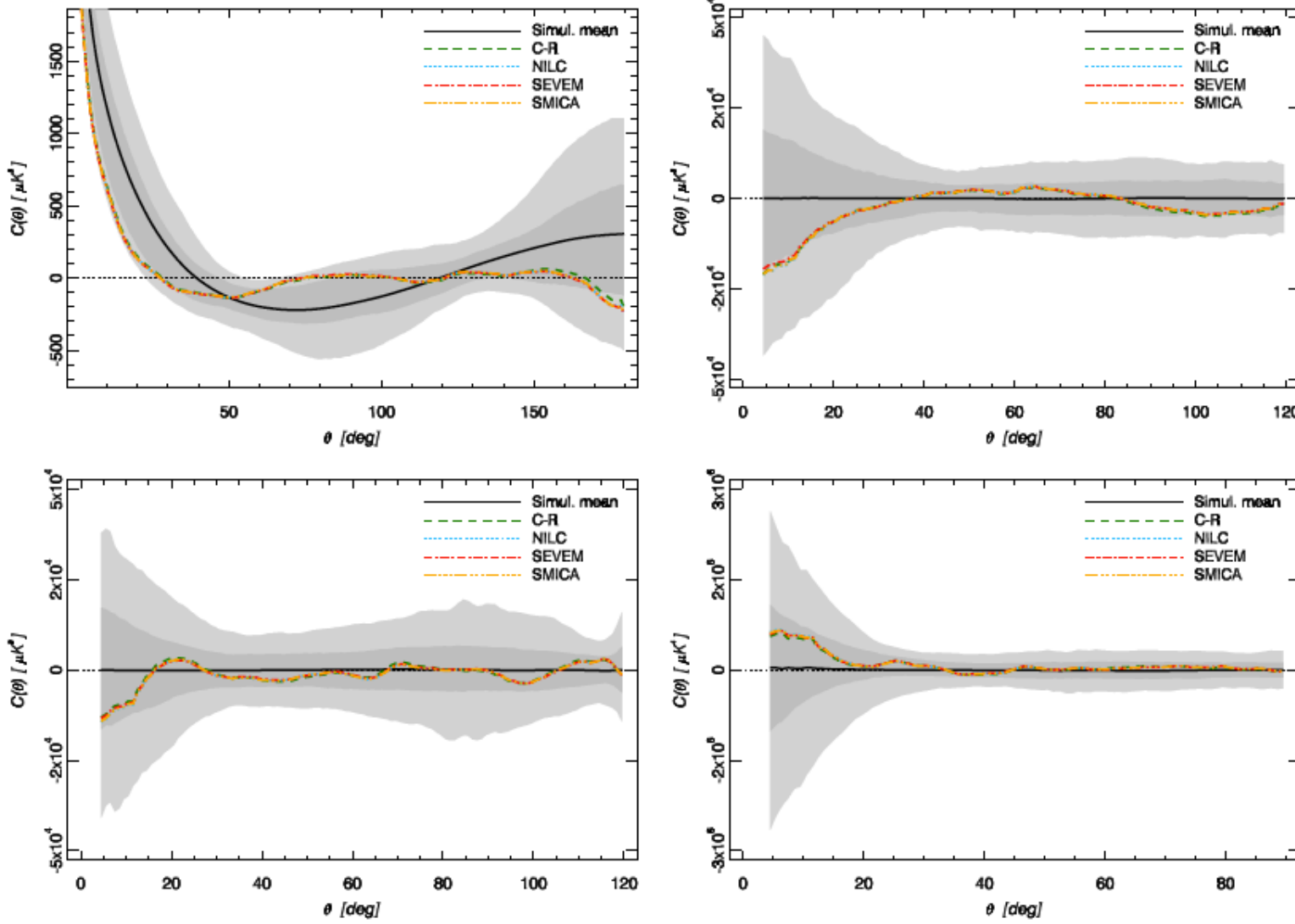
3-pt equilateral



4-pt rhombic

There are many **polynomials** that can be analysed, but we concentrate in three of them (plus the 2-point correlation function).

# N-point correlation function



# N-point correlation function

**Table 11.** Probabilities of obtaining values of the  $\chi^2$  statistic of the N-point functions shown in Fig. 9 for the *Planck* fiducial  $\Lambda$ CDM model at least as large as the observed values of the statistic for *Planck* CMB maps with resolution parameter  $N_{\text{side}} = 2048$  estimated using the C-R, NILC, SEVEM, and SMICA methods.

	C-R	NILC	SEVEM	SMICA
2-pt. . . . .	0.335	0.474	0.573	0.497
pseudo-coll. 3-pt. . . .	0.522	0.463	0.469	0.448
equil. 3-pt. . . . .	0.853	0.789	0.819	0.796
4-pt. . . . .	0.532	0.534	0.579	0.526

**Table 9.** Probabilities of obtaining values for the  $\chi^2$  statistic of the  $N$ -point functions shown in Fig. 6 for the *Planck* fiducial  $\Lambda$ CDM model at least as large as the observed values of the statistic for the *Planck* CMB maps with resolution parameter  $N_{\text{side}} = 64$  estimated using the C-R, NILC, SEVEM and SMICA methods.

	C-R	NILC	SEVEM	SMICA
2-pt. . . . .	0.883	0.859	0.884	0.855
pseudo-coll. 3-pt. . . .	0.922	0.918	0.945	0.908
equil. 3-pt. . . . .	0.962	0.966	0.978	0.968
4-pt. . . . .	0.975	0.977	0.979	0.977

No evidence of statistical deviations.

More tension at largest scales and, in particular, for the 4-point rhombic function.

However (as it will be shown latter), there is evidence of hemispherical asymmetry.

# N-point correlation function

**Table 20.** Probabilities of obtaining values of the  $\chi^2$  statistic for the *Planck* fiducial model at least as large as the observed values of the statistic for the *Planck* maps with resolution parameter  $N_{\text{side}} = 64$  estimated using the C-R, NILC, SEVEM and SMICA methods.

	C-R	NILC	SEVEM	SMICA
Two-point function				
Northern Ecliptic . . . .	0.935	0.924	0.927	0.932
Southern Ecliptic . . . .	0.633	0.599	0.639	0.592
Pseudo-collapsed three-point function				
Northern Ecliptic . . . .	1.000	1.000	1.000	1.000
Southern Ecliptic . . . .	0.349	0.310	0.381	0.301
Equilateral three-point function				
Northern Ecliptic . . . .	0.996	0.999	0.999	0.999
Southern Ecliptic . . . .	0.627	0.644	0.678	0.656
Rhombic four-point function				
Northern Ecliptic . . . .	0.999	0.999	0.999	0.999
Southern Ecliptic . . . .	0.559	0.548	0.574	0.553

Similar asymmetry manifested by the N-point correlation functions.

The 2-pt indicates less power in the northern Ecliptic hemisphere.

The 3-pt and the 4-pt show less structure in the northern hemisphere.

# Minkowski functionals

**Table 14.** Non directional Gaussianity tests using normalized Minkowski Functionals: Dependence on component separation methods.

Method	C-R	NILC	SEVEM	SMICA
$P(\chi^2 > \chi^2_{\text{Planck}})$	0.288	0.303	0.415	0.358

**Table 13.** Non-directional Gaussianity tests using normalized Minkowski Functionals: dependence of  $P(\chi^2 > \chi^2_{\text{Planck}})$  on Sky resolution.

$N_{\text{side}}$	2048	1024	512	256	128
Normalized MFs	0.358	0.356	0.245	0.225	0.223

**Table 15.** Non directional Gaussianity tests using normalized Minkowski Functionals : Sky coverage.

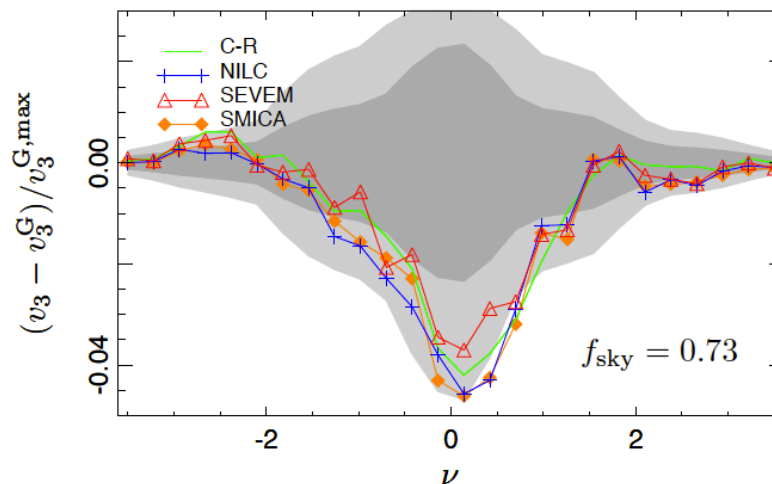
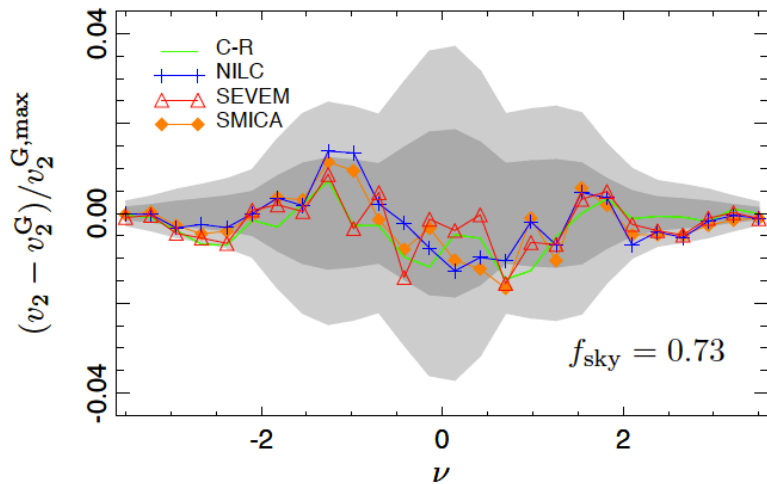
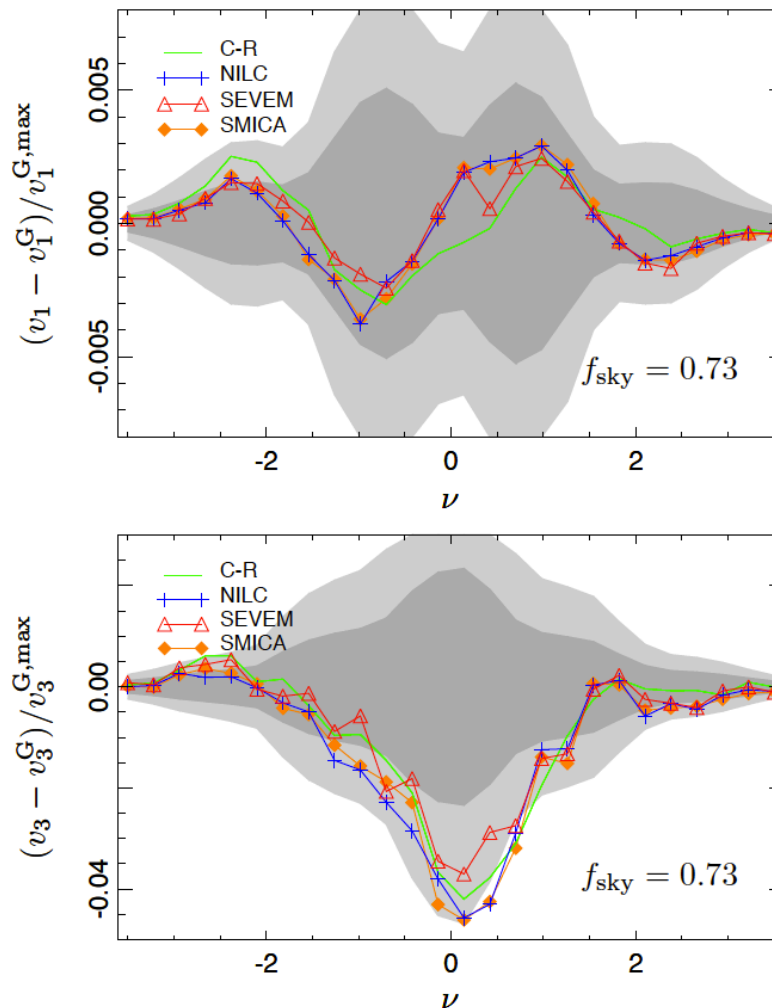
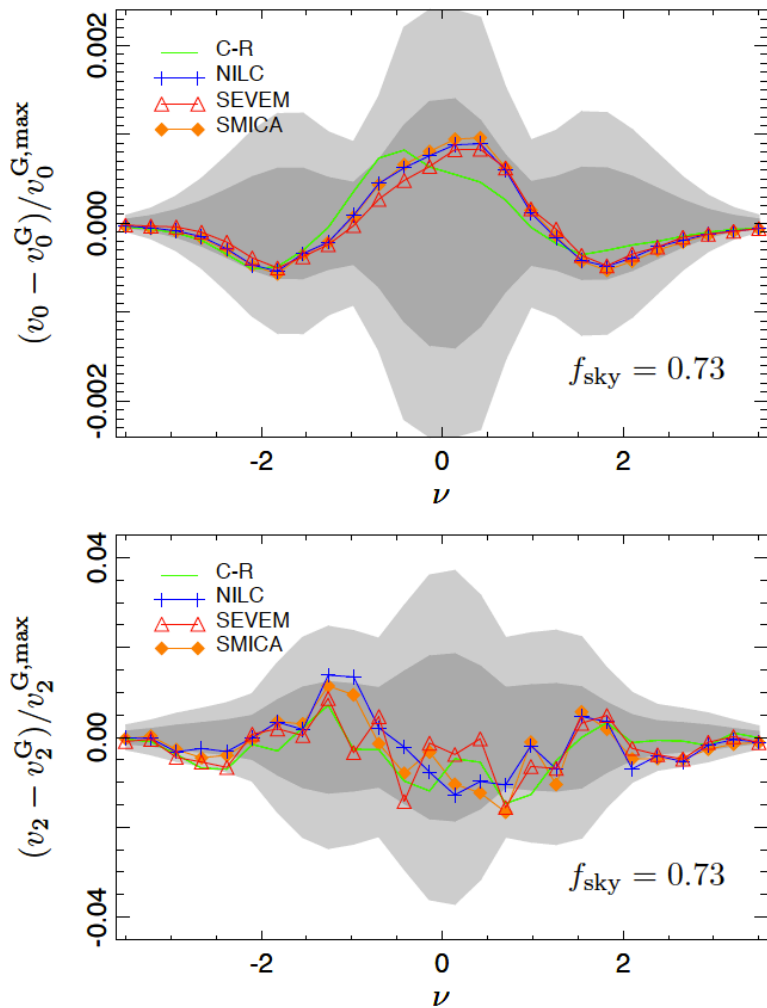
$f_{\text{sky}}$	0.73	0.62	0.46	0.23
$P(\chi^2 > \chi^2_{\text{Planck}})$	0.358	0.042	0.670	0.780

The MF describe the morphology of fields in any dimension, and have largely been used as NG and anisotropy estimators of the CMB.

They are additive for disjoint regions of the sky and invariant under rotations and translations.

No evidence of deviation found in the data

# Minkowski functionals



# Bispectrum

Three point correlator fo the  $a_{\ell m}$  coefficients:  $B_{m_1 m_2 m_3}^{\ell_1 \ell_2 \ell_3} = a_{\ell_1 m_1} a_{\ell_2 m_2} a_{\ell_3 m_3}$

Angle-averaged bispectrum:

$$B_{\ell_1 \ell_2 \ell_3} = \sum_{m_1 m_2 m_3} \binom{\ell_1 \ell_2 \ell_3}{m_1 m_2 m_3} B_{m_1 m_2 m_3}^{\ell_1 \ell_2 \ell_3}$$

The reduced bispectrum is normally used:  $b_{\ell_1 \ell_2 \ell_3} = h_{\ell_1 \ell_2 \ell_3}^{-1} B_{\ell_1 \ell_2 \ell_3}$

where  $h_{\ell_1 \ell_2 \ell_3}$  is a geometrical factor:  $h_{\ell_1 \ell_2 \ell_3} = \left[ \frac{(2\ell_1 + 1)(2\ell_2 + 1)(2\ell_3 + 1)}{4\pi} \right]^{1/2} \binom{\ell_1 \ell_2 \ell_3}{0 0 0}$

Two bispectrum estimators are used:

Modal

$$Q_{ijk}(\ell_1 \ell_2 \ell_3) = q_i(\ell_1) q_j(\ell_2) q_k(\ell_3) + perms$$

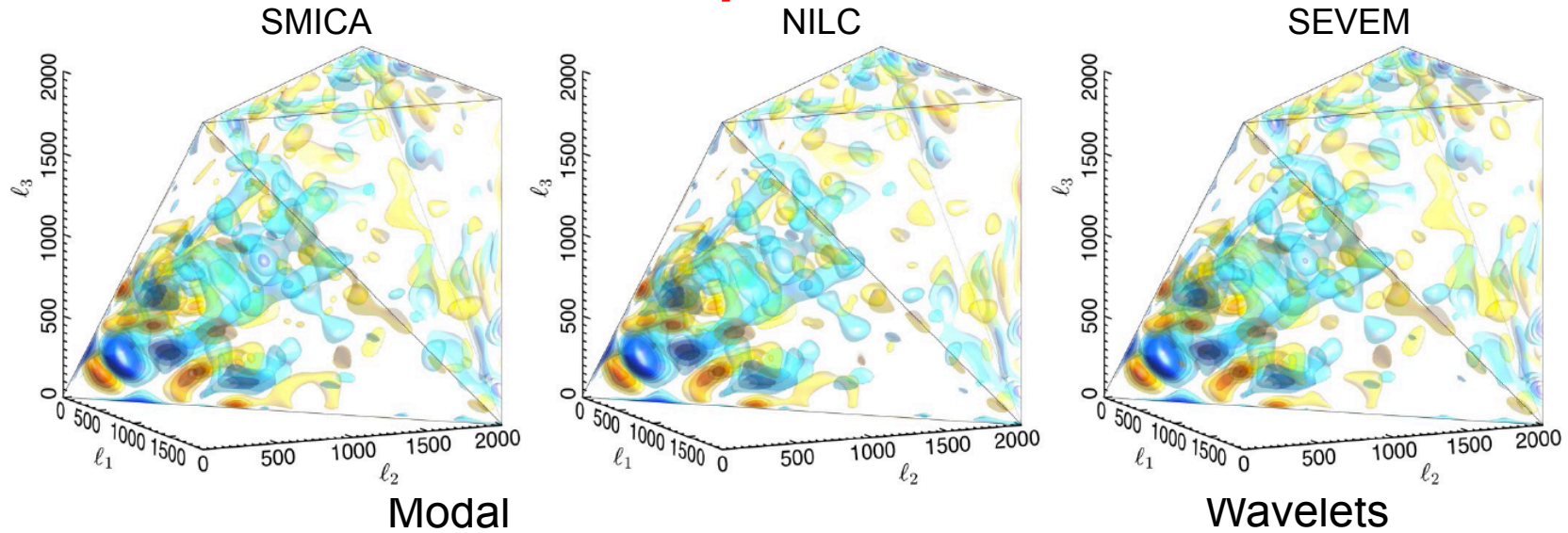
$$\frac{b_{\ell_1 \ell_2 \ell_3}}{(C_{\ell_1} C_{\ell_2} C_{\ell_3})^{1/2}} = \sum_n \beta_{ijk} Q_{ijk}(\ell_1 \ell_2 \ell_3)$$

Wavelets

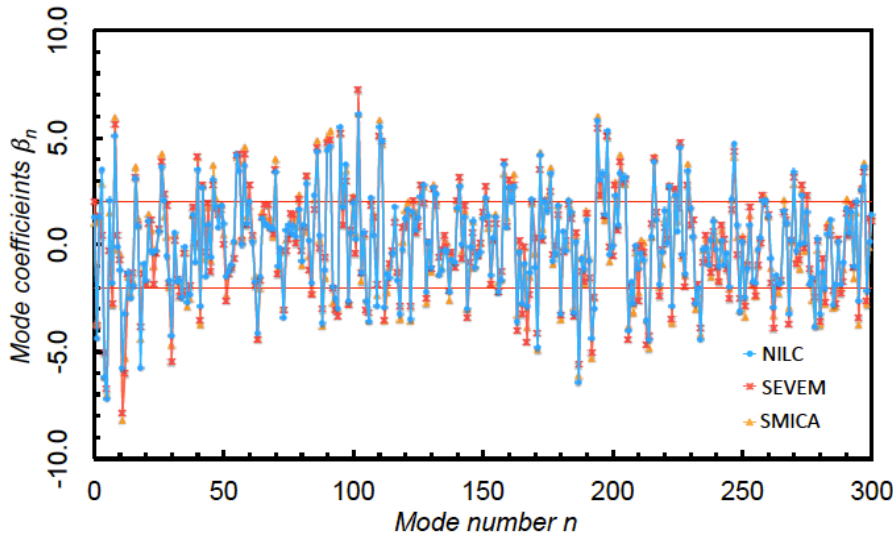
$$q_{ijk} = \frac{1}{\sigma_i \sigma_j \sigma_k} \int w(\vec{b}, R_i) w(\vec{b}, R_j) w(\vec{b}, R_k) d\vec{b}$$

$$\chi^2(f_{nl}) = \sum_{ijk,rst} (q_{ijk} - \langle q_{ijk} \rangle_{f_{nl}}) C_{ijk,rst}^{-1} (q_{rst} - \langle q_{rst} \rangle_{f_{nl}})$$

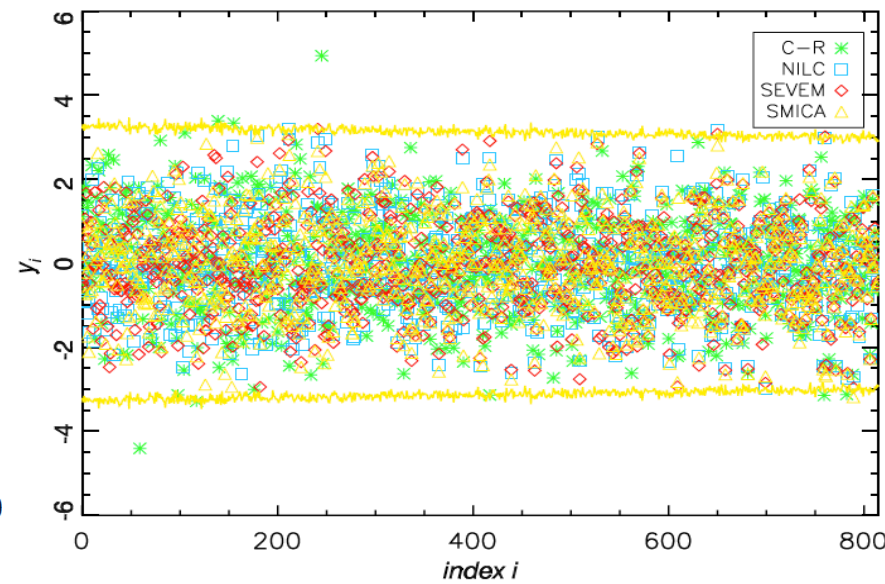
# Bispectrum



Modal



Wavelets



No evidence of deviations from the null hypothesis

# Wavelet statistics

Spherical Mexican Hat Wavelet coefficients:

$$\omega_T(R, p) = \sum_{\ell=0}^{\ell_{\max}} \sum_{m=-\ell}^{m=\ell} t_{\ell m} W_{\ell}^{\text{SMHW}}(R) Y_{\ell m}(p) \quad t_{\ell m} = \int d\Omega Y_{\ell m}^*(p) T(p)$$

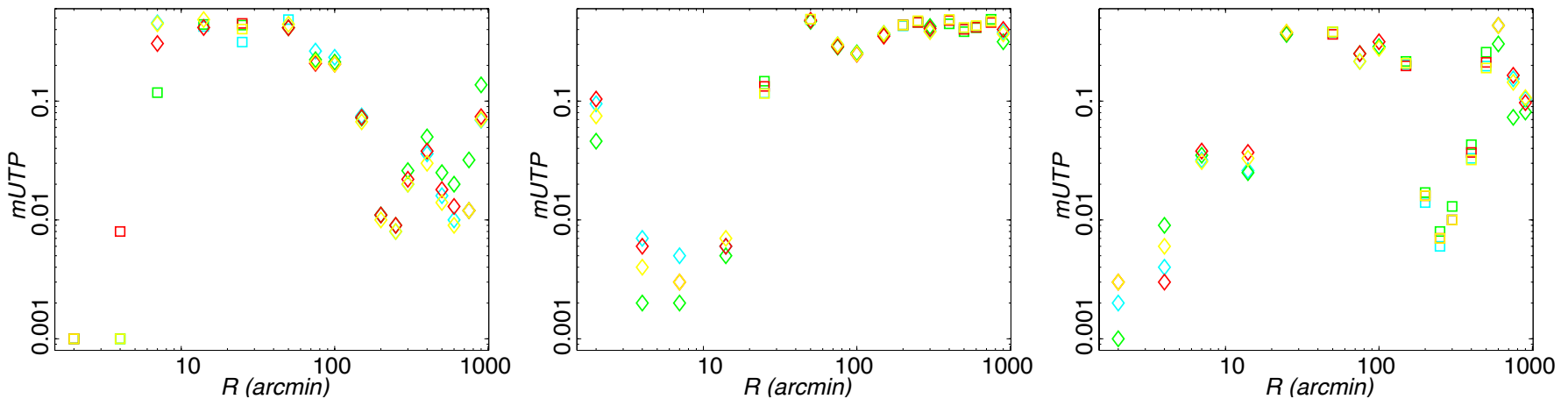


**Fig. 13.** Standard deviation (left), skewness (centre) and kurtosis (right) of the SMHW coefficients as a function of the wavelet scale  $R$ . Results are given for the four *Planck* CMB maps (green: Commander-Ruler, light-blue: NILC; red: SEVEM; yellow: SMICA). Modified upper tail probabilities ( $mUTP$ , see text for details) are obtained by comparing with 1000 simulations processed through the component separation pipelines. Squares represent modified upper tail probabilities that correspond to an actual upper tail probability above 0.5; diamonds represent upper tail probabilities below 0.5.

# Wavelet statistics

Spherical Mexican Hat Wavelet coefficients:

$$\omega_T(R, p) = \sum_{\ell=0}^{\ell_{\max}} \sum_{m=-\ell}^{m=\ell} t_{\ell m} W_{\ell}^{\text{SMHW}}(R) Y_{\ell m}(p) \quad t_{\ell m} = \int d\Omega Y_{\ell m}^*(p) T(p)$$

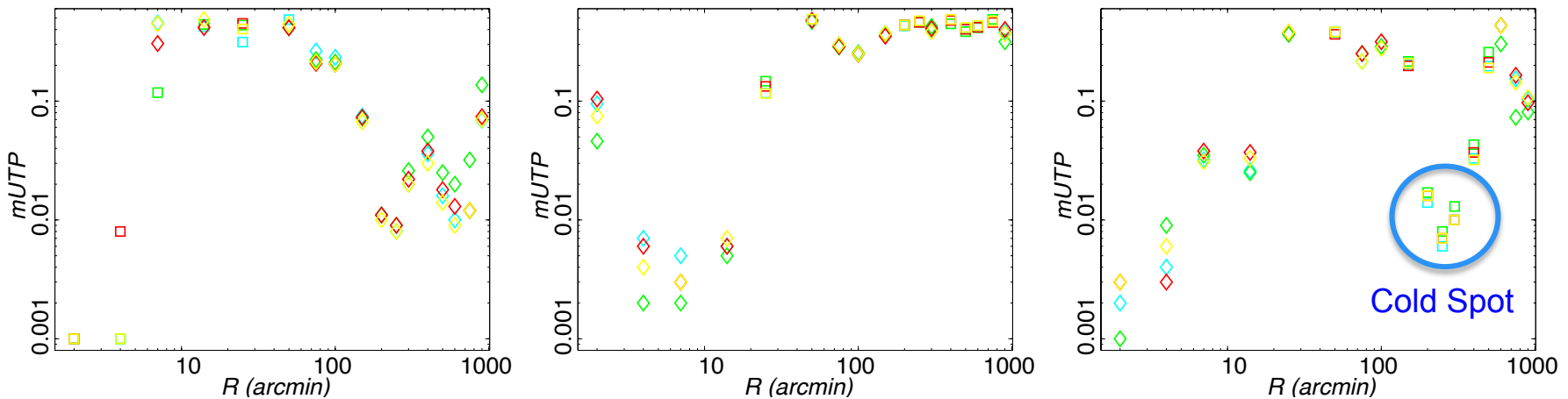


**Fig. 13.** Standard deviation (left), skewness (centre) and kurtosis (right) of the SMHW coefficients as a function of the wavelet scale  $R$ . Results are given for the four *Planck* CMB maps (green: Commander-Ruler, light-blue: NILC; red: SEVEM; yellow: SMICA). Modified upper tail probabilities ( $mUTP$ , see text for details) are obtained by comparing with 1000 simulations processed through the component separation pipelines. Squares represent modified upper tail probabilities that correspond to an actual upper tail probability above 0.5; diamonds represent upper tail probabilities below 0.5.

# Wavelet statistics

Spherical Mexican Hat Wavelet coefficients:

$$\omega_T(R, p) = \sum_{\ell=0}^{\ell_{\max}} \sum_{m=-\ell}^{m=\ell} t_{\ell m} W_{\ell}^{\text{SMHW}}(R) Y_{\ell m}(p) \quad t_{\ell m} = \int d\Omega Y_{\ell m}^*(p) T(p)$$

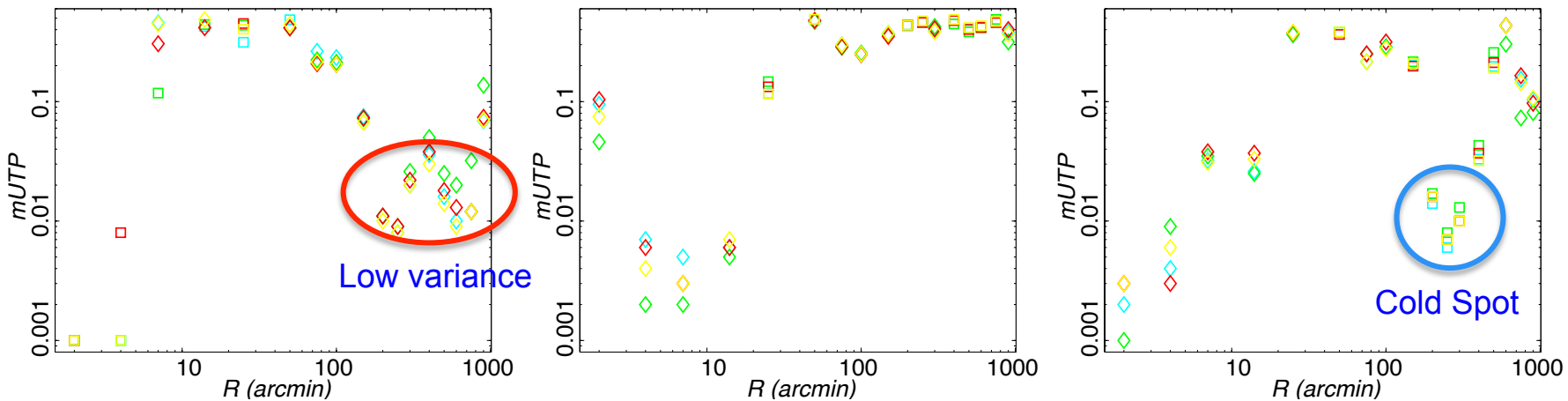


**Fig. 13.** Standard deviation (left), skewness (centre) and kurtosis (right) of the SMHW coefficients as a function of the wavelet scale  $R$ . Results are given for the four *Planck* CMB maps (green: Commander-Ruler, light-blue: NILC; red: SEVEM; yellow: SMICA). Modified upper tail probabilities ( $mUTP$ , see text for details) are obtained by comparing with 1000 simulations processed through the component separation pipelines. Squares represent modified upper tail probabilities that correspond to an actual upper tail probability above 0.5; diamonds represent upper tail probabilities below 0.5.

# Wavelet statistics

Spherical Mexican Hat Wavelet coefficients:

$$\omega_T(R, p) = \sum_{\ell=0}^{\ell_{\max}} \sum_{m=-\ell}^{m=\ell} t_{\ell m} W_{\ell}^{\text{SMHW}}(R) Y_{\ell m}(p) \quad t_{\ell m} = \int d\Omega Y_{\ell m}^*(p) T(p)$$

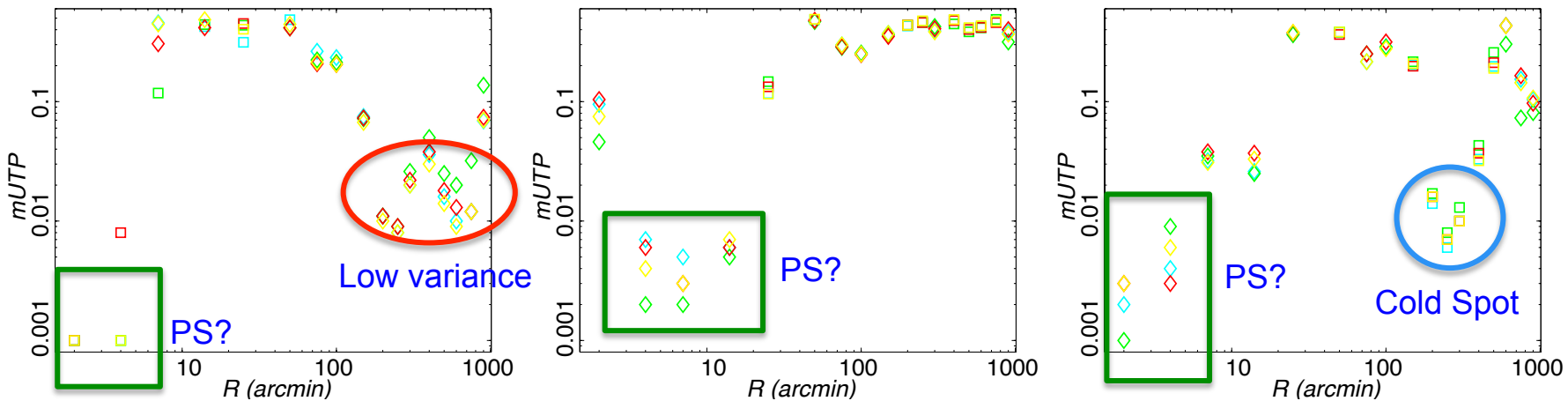


**Fig. 13.** Standard deviation (left), skewness (centre) and kurtosis (right) of the SMHW coefficients as a function of the wavelet scale  $R$ . Results are given for the four *Planck* CMB maps (green: Commander-Ruler, light-blue: NILC; red: SEVEM; yellow: SMICA). Modified upper tail probabilities ( $mUTP$ , see text for details) are obtained by comparing with 1000 simulations processed through the component separation pipelines. Squares represent modified upper tail probabilities that correspond to an actual upper tail probability above 0.5; diamonds represent upper tail probabilities below 0.5.

# WMAP anomalies revisited

- Several of the most important anomalies detected by WMAP are considered:
  - Mode alignment
  - Low variance
  - Hemispherical asymmetry
  - The Cold Spot

# Multipole alignment

The direction of a given multipole is estimated by maximizing its angular momentum dispersion:

$$\sum_m m^2 |a_{lm}(n)|^2$$

(e.g., de Oliveira-Costa et al. 2004)  
→ axes determination (headless vector)

The quadrupole / octopole alignment in Planck data is within 10 degrees (as compared to the 3 degrees reported in WMAP 9yr), and is less significant (approx 3%).

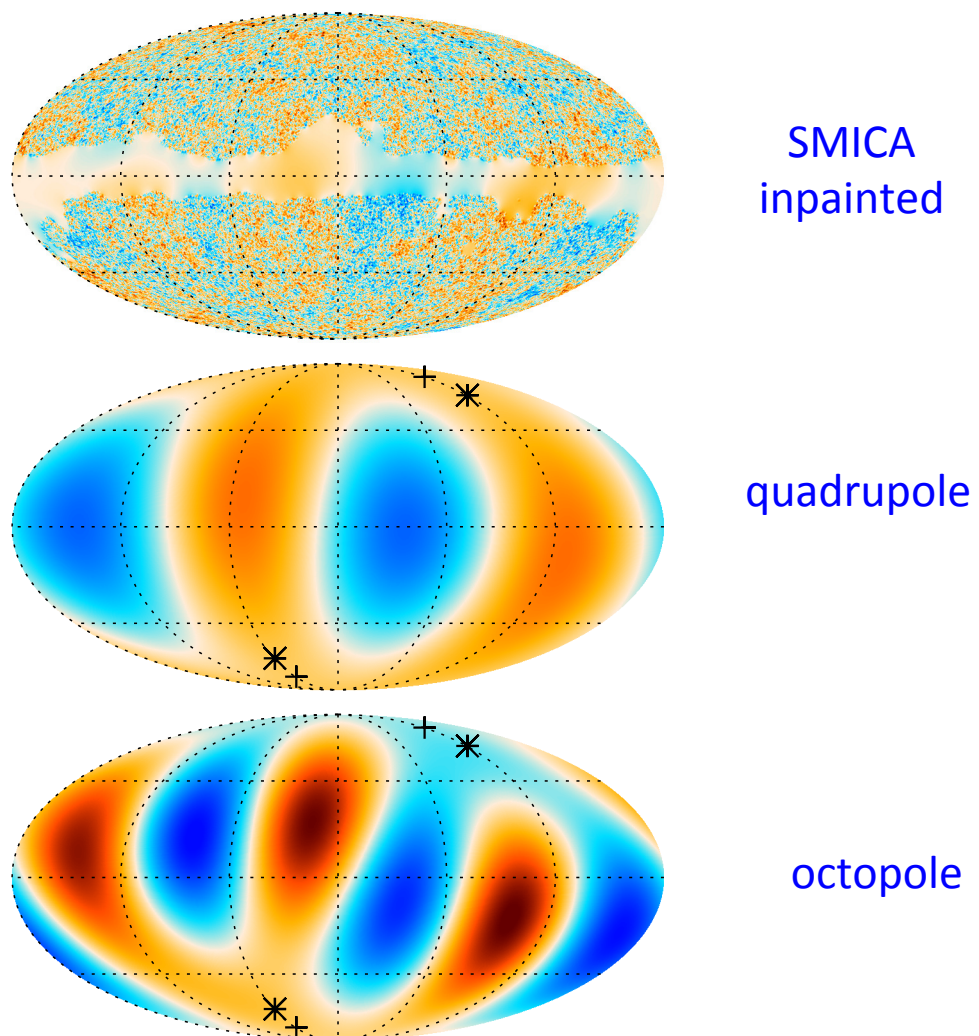


**Fig. 20.** Upper: The Wiener filtered SMICA CMB sky (temperature range  $\pm 400 \mu\text{K}$ ). Middle: the derived quadrupole (temperature range  $\pm 35 \mu\text{K}$ ). Lower: the derived octopole (temperature range  $\pm 35 \mu\text{K}$ ). Cross and star signs indicate axes of the quadrupole and octopole, respectively, around which the angular momentum dispersion is maximized.

# Low variance

**Table 18.** Lower tail probability for the variance, skewness and kurtosis at  $N_{\text{side}} = 16$ , using different masks.

Mask	C-R	NILC	SEVEM	SMICA
Variance				
U73, $f_{\text{sky}} = 78\%$ . . . . .	0.019	0.017	0.014	0.019
CL58, $f_{\text{sky}} = 58\%$ . . . . .	0.004	0.003	0.003	0.003
CL37, $f_{\text{sky}} = 37\%$ . . . . .	0.028	0.017	0.018	0.016
Ecliptic North, $f_{\text{sky}} = 39\%$ . . . .	0.001	0.001	0.001	0.002
Ecliptic South, $f_{\text{sky}} = 39\%$ . . . .	0.464	0.479	0.454	0.490
Skewness				
U73, $f_{\text{sky}} = 78\%$ . . . . .	0.016	0.015	0.023	0.012
CL58, $f_{\text{sky}} = 58\%$ . . . . .	0.208	0.139	0.162	0.147
CL37, $f_{\text{sky}} = 37\%$ . . . . .	0.517	0.467	0.503	0.469
Ecliptic North, $f_{\text{sky}} = 39\%$ . . . .	0.502	0.526	0.526	0.521
Ecliptic South, $f_{\text{sky}} = 39\%$ . . . .	0.004	0.006	0.008	0.004
Kurtosis				
U73, $f_{\text{sky}} = 78\%$ . . . . .	0.972	0.973	0.966	0.982
CL58, $f_{\text{sky}} = 58\%$ . . . . .	0.630	0.726	0.711	0.711
CL37, $f_{\text{sky}} = 37\%$ . . . . .	0.069	0.135	0.130	0.124
Ecliptic North, $f_{\text{sky}} = 39\%$ . . . .	0.094	0.229	0.196	0.245
Ecliptic South, $f_{\text{sky}} = 39\%$ . . . .	0.933	0.916	0.886	0.948

As already seen in WMAP data, the variance of the data is lower than expected.

In addition, large scale analysis shows that also the skewness (and, at a less extend the kurtosis), also exhibit an anomalous behaviour.

Even more, these quantities are also sensible to the hemispherical asymmetry, expressed in terms of the Ecliptic plane.

# Low variance

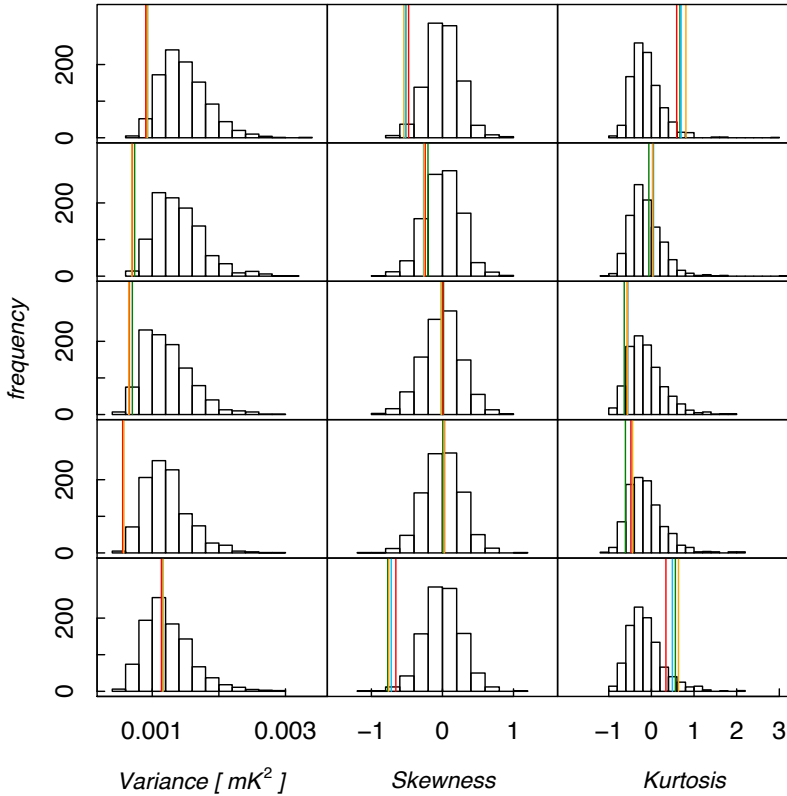


**Fig. 21.** Variance, skewness and kurtosis at  $N_{\text{side}} = 16$ , for the U73 mask, CL58, CL37, ecliptic North and ecliptic South (from top to bottom). The different lines represent the four component separation methods C-R (green), NILC (blue), SEVEM (red), and SMICA (orange).

The low variance could be related to the largest scales anomalies: notice that the cosmological parameter determination is mostly dominated by multipoles  $> 50$ , while the variance is more affected by the low multipoles.

Therefore, a mismatch between the data and the simulations at these scales will be reflected in the variance.

In fact, after removal of the quadrupole and the octopole from the data, the three statistics are more compatible with the data.

However, the asymmetry problems persists...

# Dipolar asymmetry

## 1<sup>st</sup> approach: Power asymmetry

It provides a non-parametric approach to determine a dipolar anisotropy:

1. Compute the power spectrum of the CMB from the cross-correlation of the half-ring maps (a la MASTER), into 768 discs centred in the  $N_{\text{side}} = 8$  pixels
2. The 768 spectra are binned in 16 blocks of around 100 multipoles
3. The same is made with simulations. At each disc and at each 100-multipole block, the power from the simulations is subtracted and the result divided by the standard deviation.
4. Each block has now an associated map at  $N_{\text{side}} = 8$ . The dipole direction of each map is estimated, and the alignment among all the dipole directions of the different 100-multipole blocks is identified as the dipole asymmetry (for isotropic skies, each block should have an independent dipole direction).

# Dipolar asymmetry

## 1<sup>st</sup> approach: Power asymmetry

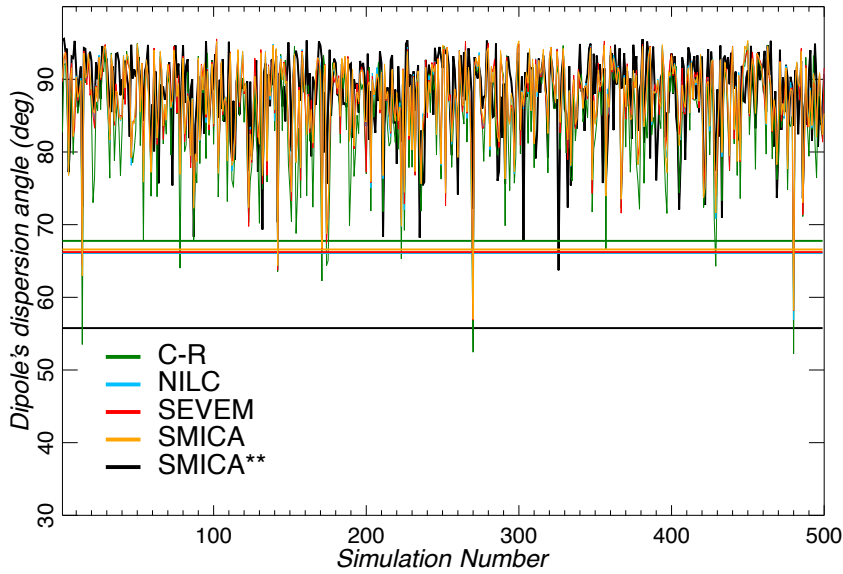


**Fig. 26.** Dispersion angles of the power spectra dipole directions, the mean of the differences of the dipole direction angles, up to  $\ell_{\max} = 1500$ , of the 500 FFP6 simulations compared to the *Planck* data with different foreground cleaning methods. All analyses, except SMICA\*\*, are performed with the U73 mask. The SMICA\*\* case is for SMICA data with the CS-SMICA89 mask.

**Table 22.** Summary of the power dipole directions on the sky, up to  $\ell_{\max} = 1500$ , as determined from maps of the power spectrum estimated from 768  $22.5^\circ$  radius discs and averaged over  $\Delta\ell = 100$  bins. The significance of the power asymmetry, shown in the last column, is quantified by the fraction of simulations that have smaller clustering of the dipole directions than the data. For the *Planck* analysis we used the 500 FFP6 simulations, while for *WMAP* we used 10000 Gaussian simulations.

Method	Mask	$(l,b)$ [°]	$\theta_{\text{mean}}^d$ [°]	Frac. $\theta_{\text{mean}}^{\text{sim}} < \theta_{\text{mean}}^d$
C-R	U73	(231, -5)	67.8	11/500
NILC	U73	(223, -1)	66.1	4/500
SEVEM	U73	(224, 2)	66.6	4/500
SMICA	U73	(225, 1)	66.2	4/500

# Dipolar asymmetry

## 1<sup>st</sup> approach: Power asymmetry

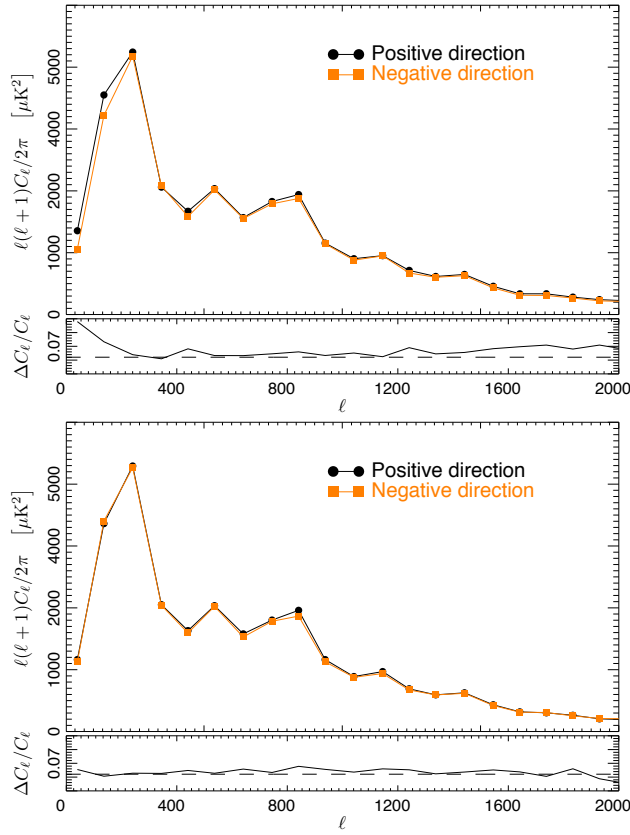


**Fig. 28.** Top: The power spectra calculated on discs with diameter  $90^\circ$  for the range  $\ell = 2 - 1500$  in the direction of maximal asymmetry and its opposite. Bottom: The equivalent plot for the direction defined by the cosmological dipole. The lower panels indicate the normaised difference of the spectra from opposing directions.

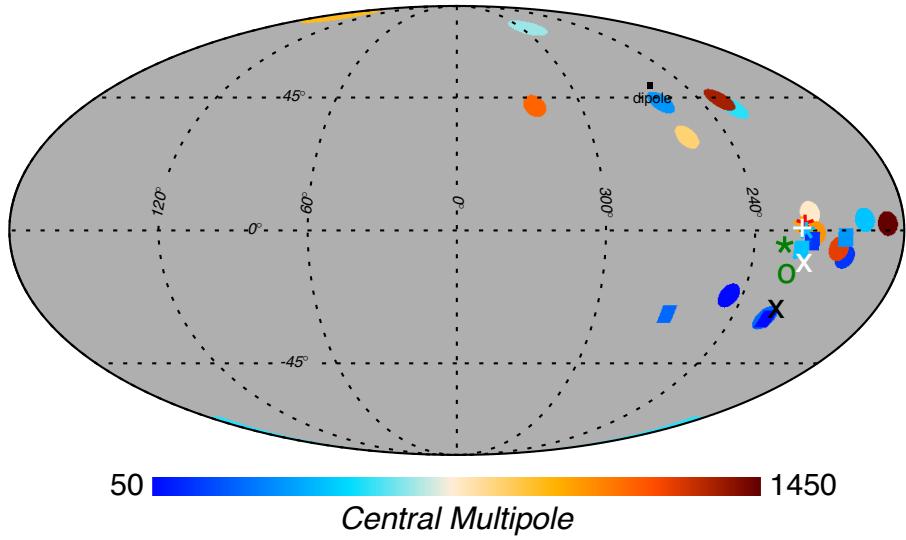


**Fig. 27.** Dipole directions for 100-multipole bins of the local power spectrum distribution from  $\ell = 2 - 1500$  in the SMICA map with the CS-SMICA89 mask applied. We also show the total direction for  $\ell_{\max} = 600$  for WMAP9 (black X) and SMICA (white X) as well as for  $\ell_{\max} = 1500$  for SMICA (white big +). The stars with different colors correspond to C-R (green), NILC (deepskyblue), SEVEM (red) and SMICA (orange) with the U73 mask. The best fit dipole modulation direction from Sect. 5.5.2 is indicated by the white open circle.

# Dipolar asymmetry

## 2<sup>nd</sup> approach: Dipole modulation

Accounts for a specific dipolar asymmetry (cosine modulation):

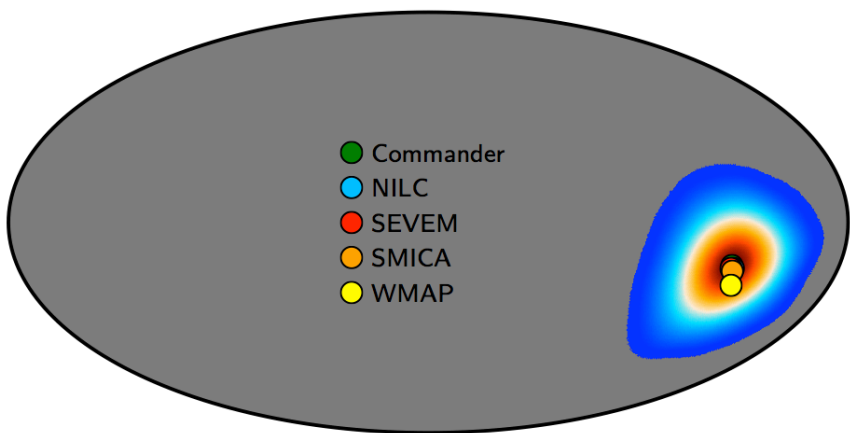
$$\mathbf{d} = (1 + A \mathbf{p} \cdot \mathbf{n}) \mathbf{s}_{\text{iso}} + \mathbf{n} \equiv \mathbf{M} \mathbf{s}_{\text{iso}} + \mathbf{n}$$

The diagram illustrates the components of the dipole modulation equation. Blue arrows point from the labels 'data', 'Modulation amplitude', 'Modulation direction', 'isotropic field', and 'noise' to the respective terms in the equation  $\mathbf{d} = (1 + A \mathbf{p} \cdot \mathbf{n}) \mathbf{s}_{\text{iso}} + \mathbf{n} \equiv \mathbf{M} \mathbf{s}_{\text{iso}} + \mathbf{n}$ .

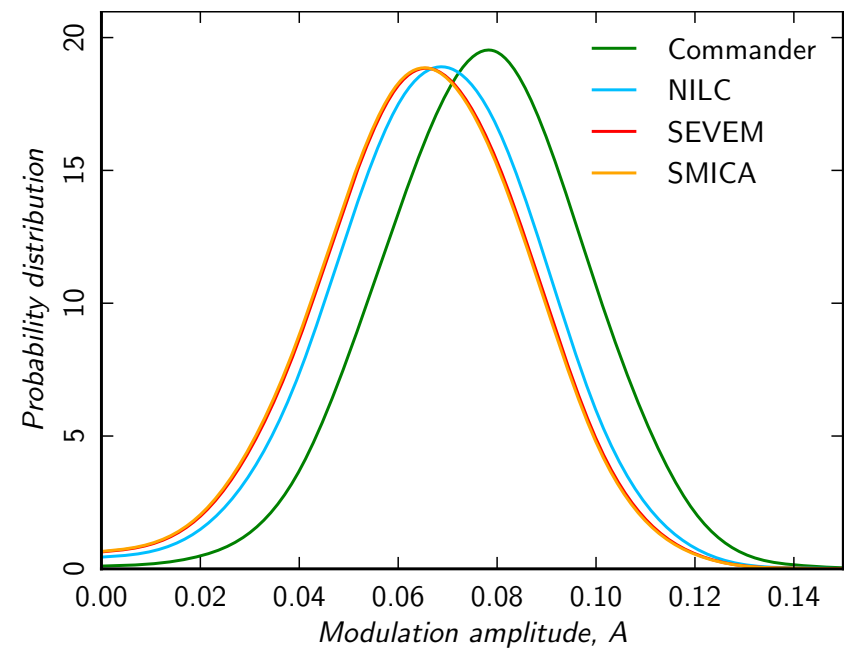
$$\mathcal{L}(A, \mathbf{p}, q, n) \propto \frac{e^{-\frac{1}{2} \mathbf{d}^T (\mathbf{M}^T \mathbf{S} \mathbf{M} + \mathbf{N} + \alpha \sum_i \mathbf{f}_i \mathbf{f}_i^T)^{-1} \mathbf{d}}}{\sqrt{|\mathbf{M}^T \mathbf{S} \mathbf{M} + \mathbf{N} + \alpha \sum_i \mathbf{f}_i \mathbf{f}_i^T|}}.$$

# Dipolar asymmetry

## 2<sup>nd</sup> approach: Dipole modulation



$$(l, b) [\text{deg}] = (227, -15) \pm 19$$



$\approx 3\sigma$  detection

# Generalized modulation

It relies on the Bipolar Spherical Harmonic (BipoSH) formalism, that is a generalization of the angular power spectrum that captures isotropy violation.

A simple model that results in the violation of statistical isotropy arises from the modulation of the CMB (but not necessary a cosine/dipolar modulation):

$$T(\mathbf{n}) = T_0(\mathbf{n})(1 + M(\mathbf{n}))$$

where the modulation is assumed to be weak, with quadratic terms neglected.

# Generalized modulation

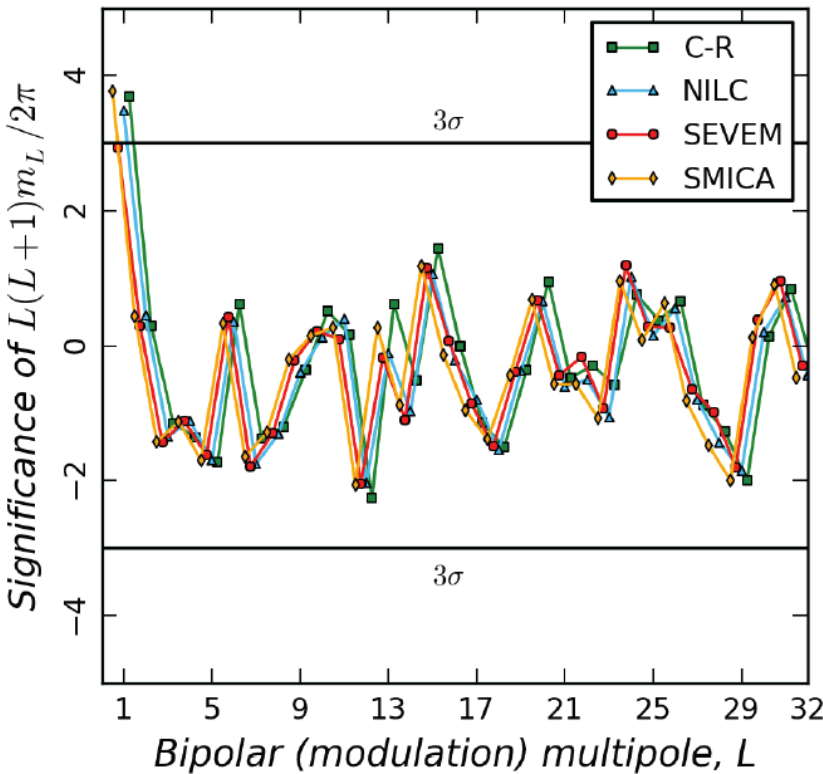


**Table 24.** This table lists the amplitude and direction of the dipole modulation in Galactic coordinates. The measured values of the dipole amplitude and direction are consistent for all maps. The corresponding dipole power for the SMICA map is seen at a detection significance of  $3.7\sigma$  as shown in Fig. 32.

Map	Dipole Amplitude	$(l,b)$ [°]
	A	$(\sigma_l = 15.4, \sigma_b = 15.1)$
C-R . . . . .	$0.072_{-0.01}^{+0.01}$	(218.9, -21.4)
NILC . . . . .	$0.070_{-0.01}^{+0.01}$	(220.3, -20.2)
SEVEM . . . . .	$0.065_{-0.011}^{+0.011}$	(221.7, -21.4)
SMICA . . . . .	$0.073_{-0.01}^{+0.01}$	(217.5, -20.2)

Only evidence of deviation for  $L=1$ , i.e.,  
a dipolar modulation

# Cold Spot

The Cold Spot was identified as an anomalous cold and large spot in the southern hemisphere of WMAP data.

It accounts for a fraction of the anomalous kurtosis of the SMHW coefficients, but it appears more robust (against masking and foreground removal) when seen through the area of the wavelet coefficients above a given threshold.

**Cold area**       $A_R^{-\nu} \equiv \#\{\omega_T(R, p) < -\nu\}$

**Hot area**       $A_R^{+\nu} \equiv \#\{\omega_T(R, p) < +\nu\}$

# Cold Spot

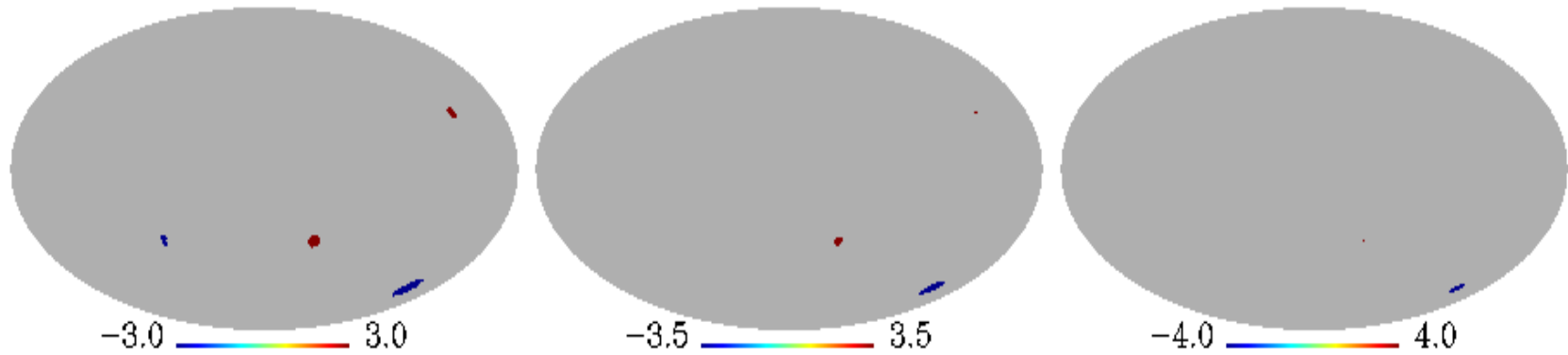


**Fig. 37.** SMHW coefficients at  $R = 300$  arc minutes, and thresholds of  $3.0\sigma$  (left),  $3.5\sigma$  (middle), and  $4.0\sigma$  (right). Results for the three masks considered in the analysis are shown: U73 mask (top), CG70 (middle) and CG60 (bottom).

**Table 25.** Upper tail probability (UTP, in %) associated to the cold (left) and hot (right) areas. Results are given for a  $\nu > 4\sigma_R$  threshold and for the four *Planck* CMB maps. The three most significant scales associated to the Cold Spot are shown. Analysis performed on the exclusions masks associated with the U73 mask.

	Scale ( $R$ ) ['']	C-R UTP (%)	NILC UTP (%)	SEVEM UTP (%)	SMICA UTP (%)
cold area	200	1.6	1.1	1.2	1.1
	250	0.3	0.3	0.3	0.3
	300	0.3	0.3	0.3	0.3
hot area	200	2.3	1.6	1.8	1.6
	250	2.7	2.2	2.4	2.2
	300	4.9	3.7	4.1	3.8

# CMB anomalies

- Many features previously detected in WMAP data are also presented in Planck, which rules out systematics as a source for them.
- There is evidence of statistical isotropy violation at least on large angular scales.
- Moreover, a dipolar power asymmetry may extend up to  $l=1500$ , while fits to a model containing a dipole modulation yield approx  $3\sigma$ .
- Evidence of departures of the spectrum at low-multipoles from the Planck fiducial ( $2.5\sigma$ )
- Which is the origin of the anomalies?
  - Solar System emission as responsible for the large scale departures?
  - Coming from the local universe, via ISW → hints of some tension reduction for some anomalies
  - Gravitational redshift (big voids) or cosmic textures responsible for the Cold Spot?

# CMB anomalies

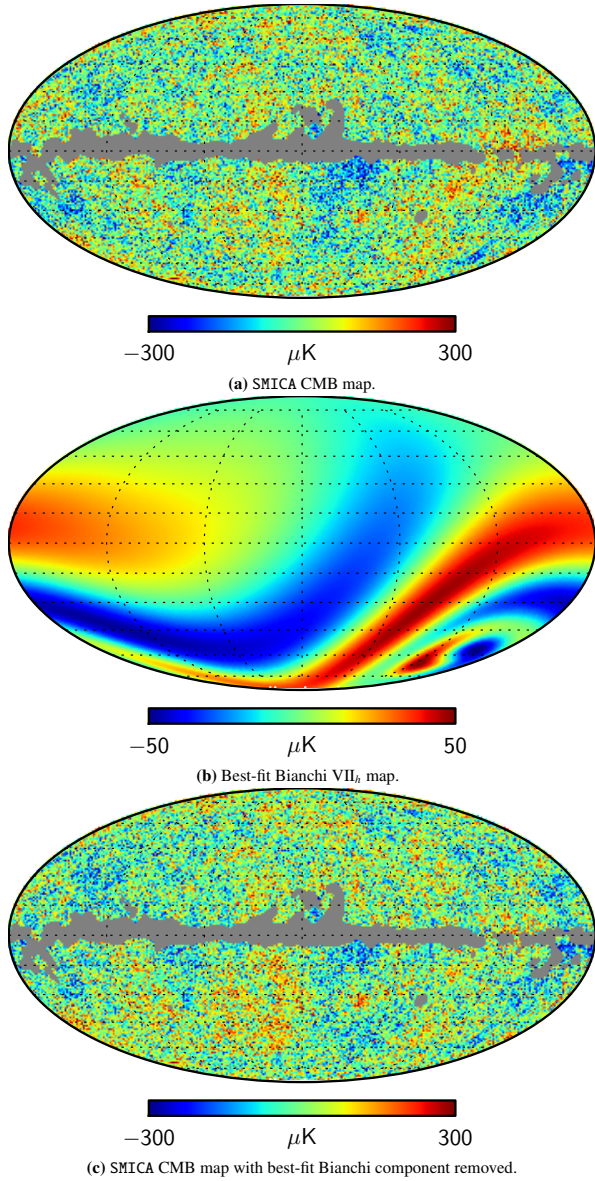
Of more interest (for us) would be that the anomalies are genuinely cosmological in origin.

In this respect, obvious candidate models include those with non-trivial topology. However, the dedicated Planck XXVI paper already shows no detection of such models (with the scale of the topology similar or larger to the diameter of the last-scattering surface).

However, this work also looks for consistency with an anisotropic Bianchi VIIh model (which already showed certain correlation with the WMAP data).

An unphysical Bianchi VIIh model actually is preferred by the data, which, ones subtracted from the data, provides a new CMB map where most of the anomalies disappear (multipole alignment, hemispherical asymmetry, the Cold Spot, ...), but not all of them (low variance). We tested that, when this model is explored properly (i.e., coupled with the cosmological estimation coming from the power spectrum) there is no evidence of it.

# CMB anomalies



Bianchi template

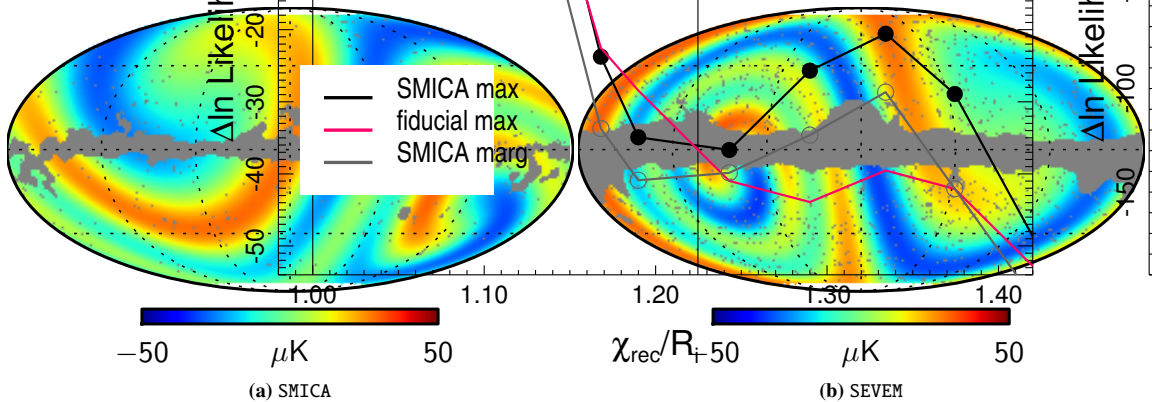


**Fig. 23:** Best-fit templates of left-handed open-coupled-Bianchi  $VII_h$  model recovered from *Planck* SMICA and SEVEM component-separated data. The Bayes factors for this model indicate that *Planck* data do not favour the inclusion of these Bianchi maps.

**Table 3:** Log-Bayes factor relative to equivalent  $\Lambda\text{CDM}$  model (positive favours Bianchi model).

Model	SMICA	SEVEM
Flat-decoupled-Bianchi (left-handed)	$2.8 \pm 0.1$	$1.5 \pm 0.1$
Flat-decoupled-Bianchi (right-handed)	$0.5 \pm 0.1$	$0.5 \pm 0.1$
Open-coupled-Bianchi (left-handed)	$0.0 \pm 0.1$	$0.0 \pm 0.1$
Open-coupled-Bianchi (right-handed)	$-0.4 \pm 0.1$	$-0.4 \pm 0.1$

# Doppler boosting of CMB fluctuations

(Planck paper XXVII)

- Our motion with respect to the CMB rest frame generates a dipole anisotropy on the sky,  $v=369 \text{ Km s}^{-1}$
- In addition, our motion also modulates and aberrates de CMB fluctuations.
- If  $T'$  and  $\hat{n}'$  are the CMB temperature and direction in the CMB frame, then the temperature in the observed frame is given by the Lorentz transformation:

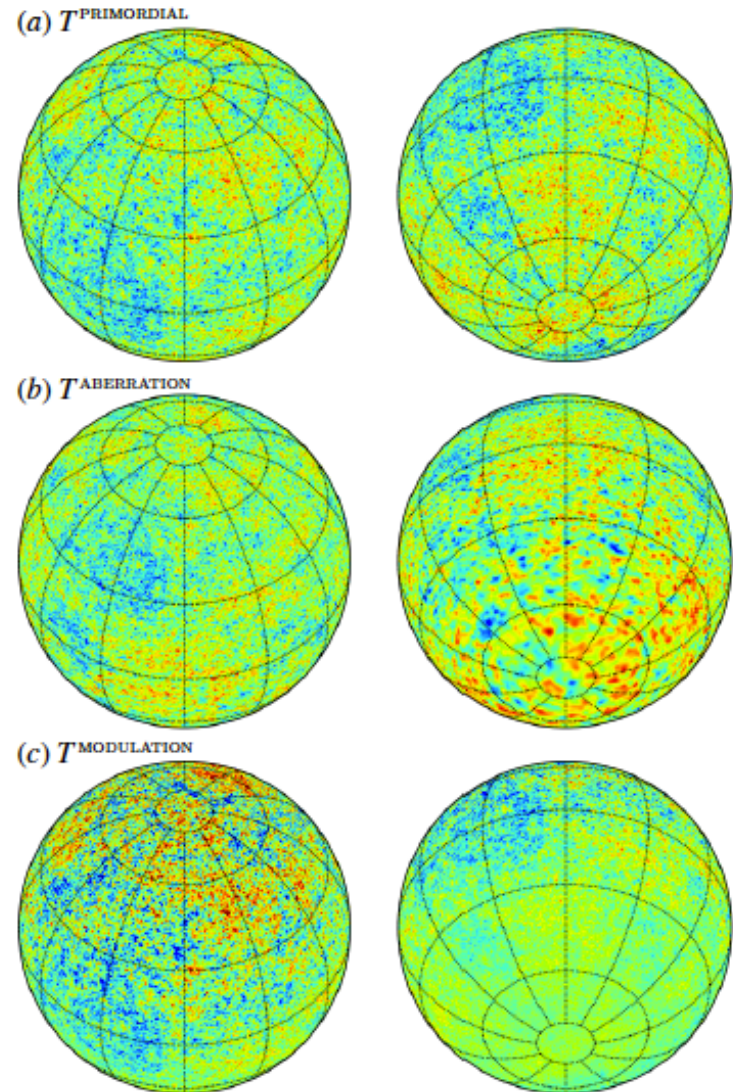
$$T(\hat{n}) = \frac{T'(\hat{n}')}{\gamma(1 - \hat{n} \cdot \beta)},$$

Where  $\hat{n} = \frac{\hat{n}' + [(\gamma - 1)\hat{n}' \cdot \hat{v} + \gamma\beta]\hat{v}}{\gamma(1 + \hat{n}' \cdot \beta)}$ ,  $\gamma \equiv (1 - \beta^2)^{-1/2}$

Expanding to linear order in  $\beta$ :

$$\delta T(\hat{n}) = \underline{T_0 \hat{n} \cdot \beta} + \underline{\delta T'(\hat{n} - \nabla(\hat{n} \cdot \beta))(1 + \hat{n} \cdot \beta)}$$

↑                   ↑                   ↑  
Dipole          Aberration          Modulation



# Doppler boosting of CMB fluctuations

- By fitting to the anisotropic template produced by the Doppler boosting a velocity is found in the known dipole direction:

$$(l, b) = (264^\circ, 48^\circ)$$

$384 \text{ km s}^{-1} \pm 78 \text{ km s}^{-1}$  (stat.)  $\pm 115 \text{ km s}^{-1}$  (syst.)

- In addition for multipoles  $\ell < 100$  the dipolar modulation anomaly is recovered.

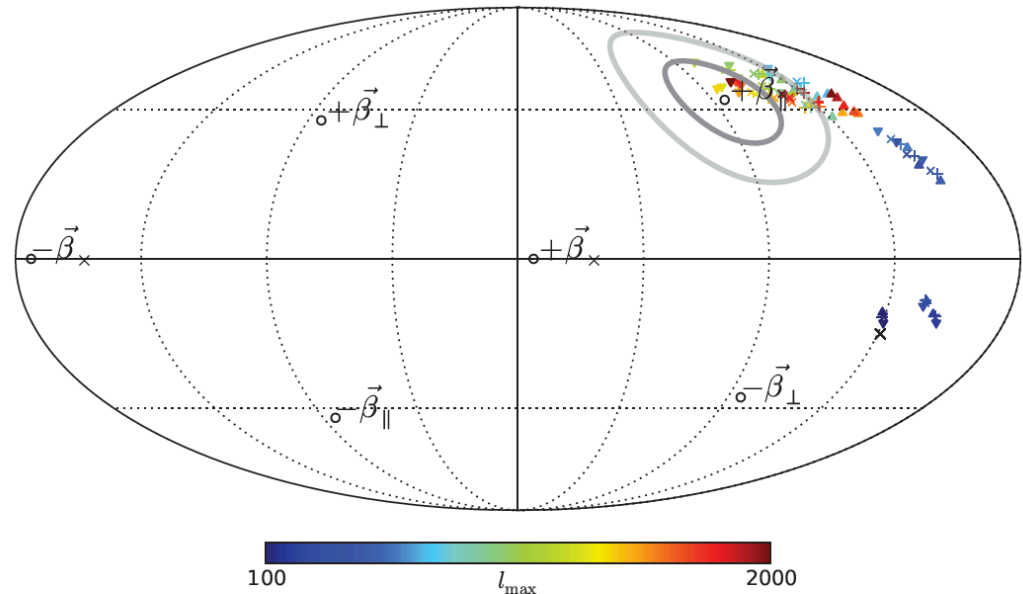
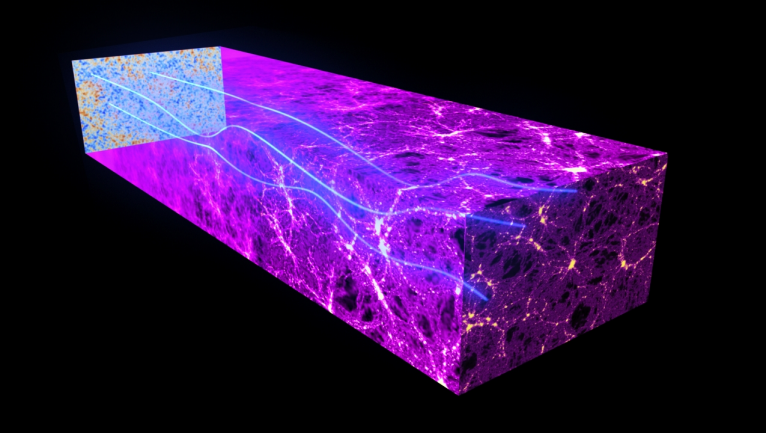


**Fig. 3.** Measured dipole direction  $\hat{\beta}$  in Galactic coordinates as a function of the maximum temperature multipole used in the analysis,  $\ell_{\max}$ . We plot the results for the four data combinations discussed in Sect. 4:  $143 \times 143$  ( $\blacktriangledown$  symbol);  $217 \times 217$  ( $\blacktriangle$  symbol);  $143 \times 217$  ( $\times$  symbol); and  $143 + 217$  ( $+$  symbol). The CMB dipole direction  $\beta_{\parallel}$  has been highlighted with  $14^\circ$  and  $26^\circ$  radius circles, which correspond roughly to our expected uncertainty on the dipole direction. The black cross in the lower hemisphere is the modulation dipole anomaly direction found for WMAP at  $\ell_{\max} = 64$  in Hoftuft et al. (2009), and which is discussed further in Planck Collaboration XXIII (2013). Note that all four estimators are significantly correlated with one another, even the  $143 \times 143$  and  $217 \times 217$  results, which are based on maps with independent noise realizations. This is because a significant portion of the dipole measurement uncertainty is from sample variance of the CMB fluctuations, which is common between channels.

# The ISW-lensing bispectrum



$$B_{\ell_1 \ell_2 \ell_3}^{m_1 m_2 m_3} \equiv \langle a_{\ell_1 m_1} a_{\ell_2 m_2} a_{\ell_3 m_3} \rangle = \langle a_{\ell_1 m_1}^P a_{\ell_2 m_2}^L a_{\ell_3 m_3}^{\text{ISW}} \rangle + 5 \text{ perm.}$$

$$B_{\ell_1 \ell_2 \ell_3}^{m_1 m_2 m_3 (\text{ISW-L})} = \mathcal{G}_{\ell_1 \ell_2 \ell_3}^{m_1 m_2 m_3} b_{\ell_1 \ell_2 \ell_3}^{\text{ISW-L}}$$

$$\begin{aligned} b_{\ell_1 \ell_2 \ell_3}^{\text{ISW-L}} &= \frac{\ell_1(\ell_1 + 1) - \ell_2(\ell_2 + 1) + \ell_3(\ell_3 + 1)}{2} \\ &\times \tilde{C}_{\ell_1}^{\text{TT}} C_{\ell_3}^{\text{T}\phi} + (\text{5 perm.}) . \end{aligned}$$

The CMB lensing and the ISW are correlated: both are caused by the matter gravitational potential. Planck provided the first detection of the ISW via this correlation.

**Table 2.** Amplitudes  $A^{\text{T}\phi}$ , errors  $\sigma_A$  and significance levels of the non-Gaussianity due to the ISW effect, for all component separation algorithms (C-R, NILC, SEVEM, and SMICA) and all the estimators (potential reconstruction, KSW, binned, and modal). For the potential reconstruction case, an additional minimum variance (MV) map has been considered (see [Planck Collaboration XVII 2013](#) for details).

Estimator		C-R	NILC	SEVEM	SMICA	MV		
$T\phi$	$\ell \geq 10$	$0.52 \pm 0.33$	1.5	$0.72 \pm 0.30$	2.4	$0.58 \pm 0.31$	1.9	$0.68 \pm 0.30$
	$\ell \geq 2$	$0.52 \pm 0.32$	1.6	$0.75 \pm 0.28$	2.7	$0.62 \pm 0.29$	2.1	$0.70 \pm 0.28$
KSW		$0.75 \pm 0.32$	2.3	$0.85 \pm 0.32$	2.7	$0.68 \pm 0.32$	2.1	$0.81 \pm 0.31$
binned		$0.80 \pm 0.40$	2.0	$1.03 \pm 0.37$	2.8	$0.83 \pm 0.39$	2.1	$0.91 \pm 0.37$
modal		$0.68 \pm 0.39$	1.7	$0.93 \pm 0.37$	2.5	$0.60 \pm 0.37$	1.6	$0.77 \pm 0.37$

# The ISW-lensing bispectrum

The ISW-lensing and the residual point sources bias the estimation of primordial bispectrum shapes with Planck data:

**Table 9.** Results for the  $f_{NL}$  parameters of the primordial local, equilateral, and orthogonal shapes, determined by the KSW, binned and modal estimators from the SMICA, NILC, SEVEM, and C-R foreground-cleaned maps. Both independent single-shape results and results marginalized over the point source bispectrum and with the ISW-lensing bias subtracted are reported; error bars are 68% CL.

	Independent			ISW-lensing subtracted			
	KSW	Binned	Modal	KSW	Binned	Modal	
SMICA							
Local . . . . .	$9.8 \pm 5.8$	$9.2 \pm 5.9$	$8.3 \pm 5.9$	.....	<b><math>2.7 \pm 5.8</math></b>	$2.2 \pm 5.9$	$1.6 \pm 6.0$
Equilateral . . . . .	$-37 \pm 75$	$-20 \pm 73$	$-20 \pm 77$	.....	<b><math>-42 \pm 75</math></b>	$-25 \pm 73$	$-20 \pm 77$
Orthogonal . . . . .	$-46 \pm 39$	$-39 \pm 41$	$-36 \pm 41$	.....	<b><math>-25 \pm 39</math></b>	$-17 \pm 41$	$-14 \pm 42$
NILC							
Local . . . . .	$11.6 \pm 5.8$	$10.5 \pm 5.8$	$9.4 \pm 5.9$	.....	$4.5 \pm 5.8$	$3.6 \pm 5.8$	$2.7 \pm 6.0$
Equilateral . . . . .	$-41 \pm 76$	$-31 \pm 73$	$-20 \pm 76$	.....	$-48 \pm 76$	$-38 \pm 73$	$-20 \pm 78$
Orthogonal . . . . .	$-74 \pm 40$	$-62 \pm 41$	$-60 \pm 40$	.....	$-53 \pm 40$	$-41 \pm 41$	$-37 \pm 43$
SEVEM							
Local . . . . .	$10.5 \pm 5.9$	$10.1 \pm 6.2$	$9.4 \pm 6.0$	.....	$3.4 \pm 5.9$	$3.2 \pm 6.2$	$2.6 \pm 6.0$
Equilateral . . . . .	$-32 \pm 76$	$-21 \pm 73$	$-13 \pm 77$	.....	$-36 \pm 76$	$-25 \pm 73$	$-13 \pm 78$
Orthogonal . . . . .	$-34 \pm 40$	$-30 \pm 42$	$-24 \pm 42$	.....	$-14 \pm 40$	$-9 \pm 42$	$-2 \pm 42$
C-R							
Local . . . . .	$12.4 \pm 6.0$	$11.3 \pm 5.9$	$10.9 \pm 5.9$	.....	$6.4 \pm 6.0$	$5.5 \pm 5.9$	$5.1 \pm 5.9$
Equilateral . . . . .	$-60 \pm 79$	$-52 \pm 74$	$-33 \pm 78$	.....	$-62 \pm 79$	$-55 \pm 74$	$-32 \pm 78$
Orthogonal . . . . .	$-76 \pm 42$	$-60 \pm 42$	$-63 \pm 42$	.....	$-57 \pm 42$	$-41 \pm 42$	$-42 \pm 42$

# Constraints on cosmic strings

Current NG constraints on cosmic strings are weaker than those imposed by the power spectrum. Two major reasons: small number of simulations to characterize the NG statistics, and dealing with residual point sources.

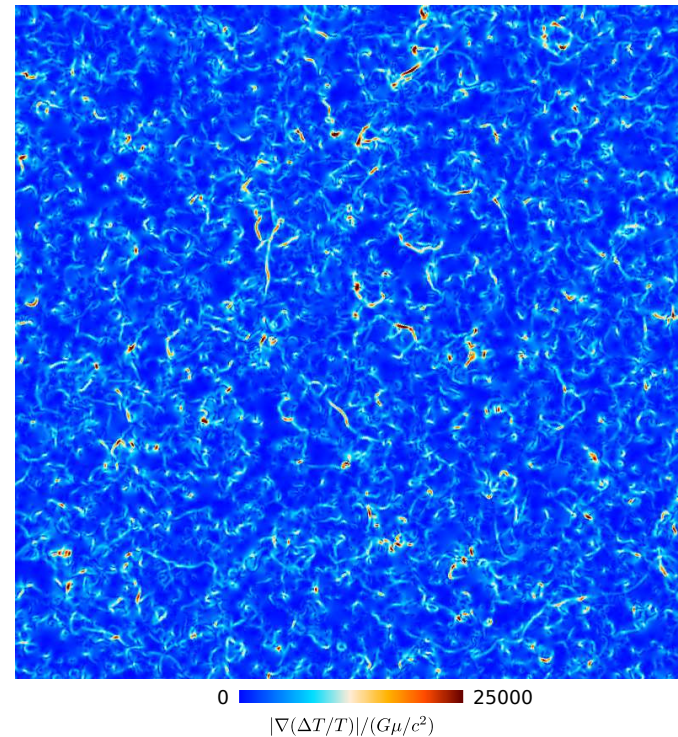
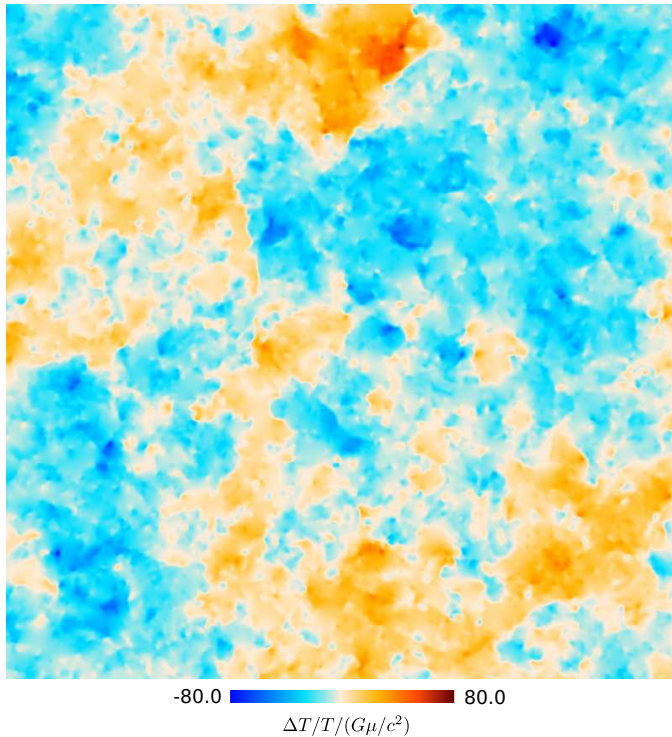


**Fig. 7.** A 20° gnomonic projection patch extracted from the full sky map and zooming into string induced temperature steps (see Fig. 6). Applying the spherical gradient magnitude operator enhances the temperature steps, and thus the string locations, even more (right).

# Constraints on cosmic strings

Current NG constraints on cosmic strings are weaker than those imposed on the power spectrum. Two major reasons: small number of simulations to characterize the NG statistics, and dealing with residual point sources.

From power spectrum analysis (95% CL)

Defect type	<i>Planck+WP</i>		<i>Planck+WP+highL</i>	
	$f_{10}$	$G\mu/c^2$	$f_{10}$	$G\mu/c^2$
NAMBU	0.015	$1.5 \times 10^{-7}$	0.010	$1.3 \times 10^{-7}$
AH-mimic	0.033	$3.6 \times 10^{-7}$	0.034	$3.7 \times 10^{-7}$
AH	0.028	$3.2 \times 10^{-7}$	0.024	$3.0 \times 10^{-7}$
SL	Semilocal	0.043	$11.0 \times 10^{-7}$	$10.7 \times 10^{-7}$
TX	Global texture	0.055	$10.6 \times 10^{-7}$	$10.5 \times 10^{-7}$

From NG analyses

Bispectrum	$G\mu/c^2 < 8.8 \times 10^{-7}$ (95% CL)
Minkowski Functionals	$G\mu/c^2 < 7.8 \times 10^{-7}$ (95% CL)

# Polarization

- Tests of Gaussianity for polarization data
- Look to the anomalies in polarization.

# Are the primordial fluctuations in polarization Gaussian and isotropic?

- Tests of Gaussianity for polarization:
  - Test the standard model
  - Validate the Gaussianity and isotropy assumption for the power spectra and cosmological parameters estimation
  - Check for systematics

# Anomalies

- Look to the anomalies in polarization
  - Either presence or absence of a specific signal provide valuable information on their nature
  - A deviation of isotropy present at recombination should be reflected in both temperature and polarization data with a correlated signal
- There are some work already done for some of the anomalies that can be directly applicable to Planck polarization data:
  - Mode alignment (Frommert & Enslin 2010)
  - Low variance (Gruppuso et al. 2013)
  - Dipolar modulation (Dvorkin et al. 2008)
  - Cold spot (Vielva et al. 2011; Fernández-Cobos et al. 2013)

# The Cold Spot in polarization

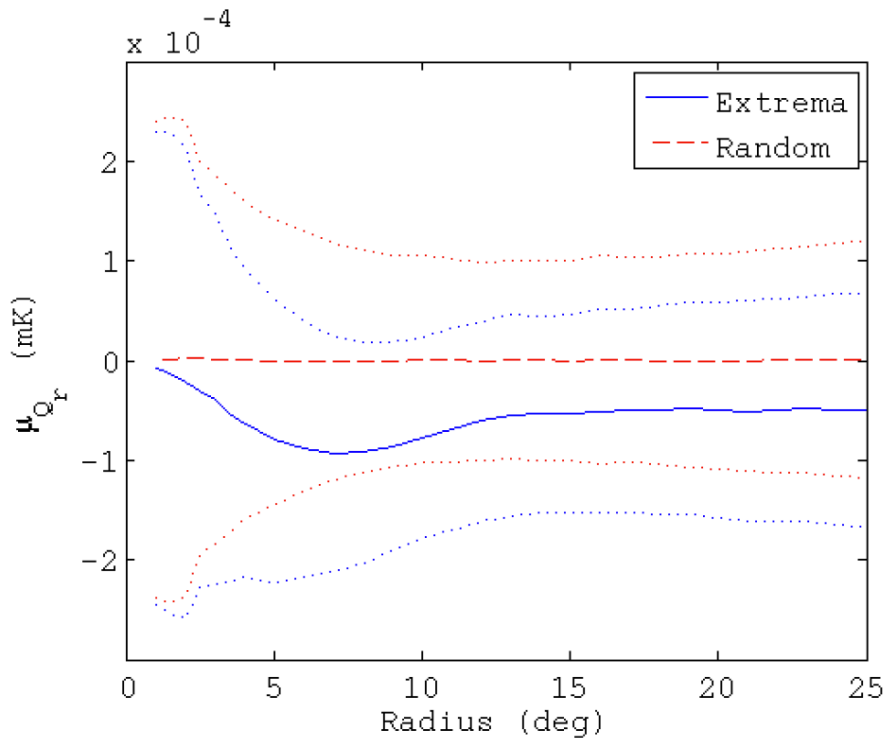
(Fernández-Cobos et al 2013)

Use the  $Q_r$  radial profile around the cold spot:

$$\mu_{Q_r}(\mathbf{x}, \theta) = \frac{1}{N_\theta} \sum_i Q_r(\mathbf{x}_i)$$

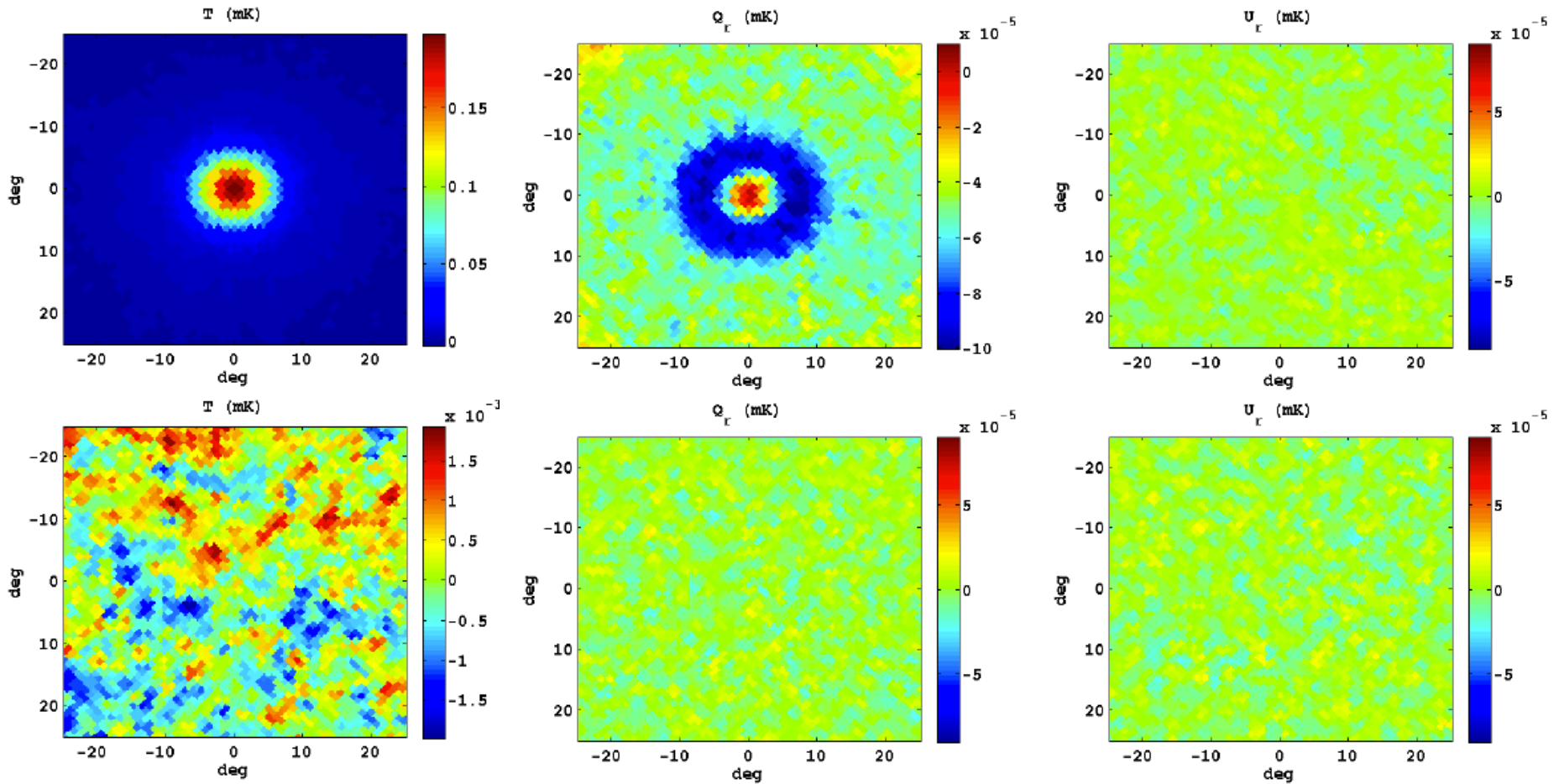
The mean value of the  $Q_r$  is related to the TE cross-power:

$$\bar{\mu}_{Q_r}(\theta) = \int f(\ell, \theta) C_\ell^{\text{TE}} d\ell$$



# The Cold Spot in polarization

(Fernández-Cobos et al 2013)



# Summary

- Expected NG signals detected:
  - ISW-lensing (at  $2.5\sigma$ )
  - Residual PS (at  $4\sigma$ )
- Only constraints on specific NG and anisotropic models:
  - primordial NG
  - cosmic strings
  - non-trivial topology and anisotropic models
- Most of the non-directional tests show overall consistency with the null hypothesis. Two important exceptions:
  - Low variance, with the low signal localized in the northern ecliptic hemisphere. Confirm with the variance of the wavelet coefficients.
  - Low variance partially connected with the low Quadrupole-octopole alignment.
  - A positive kurtosis of the wavelet coefficients connected to the Cold Spot.

# Summary

- General agreement with the anomalies found in WMAP data:
  - Anomalous low variance
  - Quadrupole-octopole alignment, although at a somewhat lower significance
  - Hemispherical asymmetry (visible up to  $l=1500$ )
  - Dipolar power modulation (also found with the generalized modulation)
  - The Cold Spot
- A bianchi template seems to fit well to most of the anomalies
- Anomalies manifest at multipoles  $< 30$  where a mismatch with the Planck best-fit power spectrum is found (at  $\approx 2.5\sigma$ )
- A satisfactory explanation for the anomalies in terms of physically motivated models is still lacking... The future is in polarization.



Planck is a project of the European Space Agency, with instruments provided by two scientific Consortia funded by ESA member states (in particular the lead countries: France and Italy) with contributions from NASA (USA), and telescope reflectors provided in a collaboration between ESA and a scientific Consortium led and funded by Denmark.